

On Modelling a Relativistic Hierarchical (Fractal) Cosmology by Tolman's Spacetime. III. Numerical Results

Marcelo B. Ribeiro ¹

Astronomy Unit
School of Mathematical Sciences
Queen Mary and Westfield College
Mile End Road
London E1 4NS
England

ABSTRACT

This paper presents numerical solutions of particular Tolman models approximating a fractal behaviour along the past light cone. The initial conditions of the numerical problem are discussed and the algorithm used to carry out the numerical integrations is presented. It was found that the numerical solutions are stiff across the flat-curved interface necessary to obtain the initial conditions of the problem. The spatially homogeneous Friedmann models are treated as special cases of the Tolman solution and solved numerically. Extending the results of paper II on the Einstein-de Sitter model, to the $K = \pm 1$ models, it was found that the open and closed Friedmann models also do not appear to remain homogeneous along the backward null cone, with a vanishing volume (average) density as one approaches the big bang singularity hypersurface. Fractal solutions, that is, solutions representing an averaged and smoothed-out single fractal, were obtained in

¹ Present address: Departamento de Astrofísica, Observatório Nacional - CNPq, Rua General José Cristino 77, Rio de Janeiro, RJ 20921, Brazil.

all three classes of the Tolman metric, but only the hyperbolic ones were found to be in agreement with observations, meaning that a possible Friedmann background universe would have to be an open one. The best fractal metric obtained through numerical simulations is also analysed in terms of evolution, homothetic self-similarity, comparison with the respective spatially homogeneous case and the fitting problem in cosmology. The paper finishes with a discussion on some objections raised by some authors against a fractal cosmology.

1 Introduction

This is the third paper of a series that studies a relativistic cosmology modelling the relativistic generalization of the single fractal Newtonian model advanced by Pietronero (1987; see also Coleman & Pietronero 1992), in which the galactic clustering problem is studied by assuming that the large-scale structure of the universe can be described as being a self-similar fractal system.²

In Ribeiro (1992a, hereafter paper I) I argued that the recent all sky redshift surveys (de Lapparent, Geller & Huchra 1986; Saunders et al. 1991) present observations consistent both with the old Charlier hypothesis of hierarchical clustering and with fractals, where the latter is in essence a more precise conceptualization of the scaling idea implicit in the hierarchical clustering hypothesis. In paper I Pietronero's (1987) basic hypotheses were assumed in order to propose similar ones in a relativistic context, and I obtained observational relations compatible with fractals in Tolman's spacetime and devised a numerical strategy for finding particular Tolman solutions representing a fractal behaviour along the backward null cone. In Ribeiro (1992b, hereafter paper II) I studied analytically the Einstein-de Sitter model in the context of the theory developed in paper I. By treating the Einstein-de Sitter model as a special case of Tolman's spacetime, I found that it does not appear to remain homogeneous along the past null geodesic, has a volume (average) density which vanishes asymptotically and that it also shows

² The models investigated in this series of papers are in the realm of classical cosmology. No hypotheses concerning inflationary cosmology have been considered.

no single fractal features along the backward null cone. The apparent inhomogeneity of the Einstein-de Sitter model is explained by the fact that densities measured along the geodesic go through different hypersurfaces of constant t , where each one has a different value for the proper density.

This paper continues the study of these cosmologies and presents relativistic fractal solutions obtained by following the numerical simulation strategy already devised in paper I. By *fractal solutions* I mean solutions where the fractal system is smoothed-out and its average density follows the de Vaucouleurs density power-law. These solutions represent fractal behaviour along the backward null cone and they were obtained for all three types of Tolman dust models, namely, elliptic, parabolic and hyperbolic. By analysing these solutions we conclude that the only ones with features that may represent real astronomical observations are of hyperbolic type. As we are studying the Tolman spacetime as a region (or regions) possibly surrounded by a Friedmann universe (see paper I), if we adopt the fitting condition approach for interpreting the match between the two spacetimes (Ellis & Stoeger 1987; Ellis & Jaklitsch 1989) we then conclude that the Friedmann background required is also hyperbolic and we would be living in an open, ever expanding, universe.

This paper is organized as follows. In §2 is shown a summary of the observational relations developed in papers I and II plus some minor extensions which will be necessary here, and in §3 I discuss the initial conditions and the algorithm used to find Tolman numerical solutions along the past light cone. In §4 I present the numerical solutions for the spatially homogeneous special cases and §5 shows fractal solutions for all types of Tolman models. §6 discusses these fractal solutions in terms of comparison with the spatially homogeneous cases, fitting condition, evolution of the most realistic fractal model in terms of real observations and relations with homothetic self-similarity. In this section I also express my criticism of criticisms of fractal cosmology. I finish in §7 with the conclusions on this and the preceding papers.

2 Observational Relations in Tolman's Dust Models

The Tolman (1934) metric for the motion of spherically symmetric dust is

$$dS^2 = dt^2 - \frac{R'^2}{f^2} dr^2 - R^2(d\theta^2 + \sin^2 \theta d\phi^2). \quad (1)$$

The Einstein field equations (with $c = G = 1$ and $\Lambda = 0$) for metric (1) reduce to a single equation

$$2R\dot{R}^2 + 2R(1 - f^2) = F, \quad (2)$$

where a dot means $\partial/\partial t$ and a prime means $\partial/\partial r$; $f(r)$ and $F(r)$ are two arbitrary functions and $R(r, t) \geq 0$. The analytical solutions of equation (2) are divided into three categories according to the values of the function $f(r)$. For $f^2 < 1$ we have the elliptic class and equation (2) has the following solution:

$$R = \frac{F(1 - \cos 2\Theta)}{4|f^2 - 1|}, \quad (3)$$

where Θ is given by

$$t + \beta = \frac{F(2\Theta - \sin 2\Theta)}{4|f^2 - 1|^{3/2}}. \quad (4)$$

For $f^2 = 1$ we have the parabolic class and the solution of equation (2) may be written as

$$R = \frac{1}{2}(9F)^{1/3}(t + \beta)^{2/3}. \quad (5)$$

Finally the hyperbolic class is given when $f^2 > 1$, and equation (2) is solved by

$$R = \frac{F(\cosh 2\Theta - 1)}{4(f^2 - 1)}, \quad (6)$$

where

$$t + \beta = \frac{F(\sinh 2\Theta - 2\Theta)}{4(f^2 - 1)^{3/2}}. \quad (7)$$

Note that one Tolman solution can have regions of differing classes, depending on the values of the function $f(r)$.

The derivatives R' , \dot{R} , \dot{R}' for the three cases above form long algebraic expressions and I shall not show them here. They can be found in paper I. The function $\beta(r)$ is a third arbitrary function which gives the local time passed since the singularity surface, that is, since the big bang. In the elliptic and hyperbolic models, it is necessary to solve equations (4) and (7) in terms of Θ so that specific values of R and its derivatives are evaluated. In order to do so numerically, we need to find the interval where the root lies. It is not difficult to show (see paper I) that in the elliptic models

$$\frac{4}{F}(t + \beta)|f^2 - 1|^{3/2} - 1 \leq 2\Theta \leq \frac{4}{F}(t + \beta)|f^2 - 1|^{3/2} + 1, \quad (8)$$

and in the hyperbolic case

$$0 < \Theta \leq \left[\frac{3}{F}(t + \beta)(f^2 - 1)^{3/2} \right]^{1/3}. \quad (9)$$

The local density in Tolman's spacetime is given by

$$8\pi\rho = \frac{F'}{2R'R^2} \quad (10)$$

and if we adopt the radius coordinate r as the parameter along the backward null cone ($r \geq 0$), we can then write the past radial null geodesic of metric (1) as

$$\frac{dt}{dr} = -\frac{R'}{f}. \quad (11)$$

The Friedmann metric is a special case of the metric (1) above, obtained when $R = a(t)g(r)$, $f = g'$ and $\beta = \text{constant}$. The usual Friedmann universe requires further that $g = \sin r$, r , $\sinh r$ and $F = b_1 \sin^3 r$, $\frac{8}{9}r^3$, $b_2 \sinh^3 r$, which are respectively the cases for $K = +1, 0, -1$. The positive constants b_1 and b_2 are scaling factors necessary to make the density parameter Ω equal to any value different from one in the open and closed models. It is also possible to show that $F(r)$ gives the gravitational mass inside the comoving radius r and $f(r)$ gives the total energy of the system also within r (see §6.1 and paper II for further details).

It was shown in paper II how the Hubble constant relates to the function $\beta(r)$ in a Einstein-de Sitter universe. It is important here to extend that result to the $K = \pm 1$ Friedmann cases. By definition, $H = \dot{R}/R = \dot{a}/a$ for constant $\beta(r)$. Considering the

especializations above, that permit us to get the Friedmann metric from the Tolman solution, and assuming $t = 0$ as our “now”, that is, $t = 0$ being the time coordinate label for the present epoch, it is straightforward to show that the present value H_0 for the Hubble constant in the closed Friedmann model is given by

$$H_0 = \frac{4 \sin 2\Theta_0}{b_1(1 - \cos 2\Theta_0)^2}, \quad (12)$$

where Θ_0 is the solution of

$$4\beta_0 = b_1(2\Theta_0 - \sin 2\Theta_0), \quad (13)$$

and $\beta(r) = \beta_0$ is a constant that gives the age of the universe. In the open Friedmann case we will have then

$$H_0 = \frac{4 \sinh 2\Theta_0}{b_2(\cosh 2\Theta_0 - 1)^2}, \quad (14)$$

and

$$4\beta_0 = b_2(\sinh 2\Theta_0 - 2\Theta_0). \quad (15)$$

It will be necessary in further calculations to obtain the value of the cosmological density parameter Ω in the Friedmann model at the present constant time hypersurface. By definition $\Omega = \rho/\rho_c$ and $\rho_c = 1/(6\pi\beta_0^2)$ at $t = 0$. Therefore, in the closed Friedmann model we have that

$$\Omega_0 = \frac{72\beta_0^2}{(b_1)^2(1 - \cos 2\Theta_0)^3}, \quad (16)$$

where Θ_0 is given by equation (13). In the open Friedmann model we have

$$\Omega_0 = \frac{72\beta_0^2}{(b_2)^2(\cosh 2\Theta_0 - 1)^3}, \quad (17)$$

with Θ_0 being the solution of equation (15).

It was shown in paper I that in a Tolman universe the redshift may be written as

$$1 + z = (1 - I)^{-1}, \quad (18)$$

where the function $I(r)$ is the solution of the differential equation

$$\frac{dI}{dr} = \frac{\dot{R}'}{f}(1 - I). \quad (19)$$

The luminosity distance d_l and the cumulative number count N_c are given by

$$d_l = R(1+z)^2, \quad (20)$$

$$N_c = \frac{1}{4M_G} \int \frac{F'}{f} dr, \quad (21)$$

where M_G is the average galactic rest mass ($\sim 10^{11} M_\odot$). The volume V of the sphere which contains the sources and the volume density (average density) ρ_v have the form

$$V = \frac{4}{3}\pi(d_l)^3, \quad (22)$$

$$\rho_v = \frac{N_c M_G}{V}. \quad (23)$$

The proposed relativistic version of Pietronero's (1987) generalized mass-length relation is given by

$$N_c = \sigma(d_l)^D \quad (24)$$

where σ is a constant related to the lower cutoff of the fractal system and D is its fractal dimension. By substituting equations (22) and (24) into equation (23) we get the de Vaucouleurs' density power law

$$\rho_v = \frac{3\sigma M_G}{4\pi} (d_l)^{-\gamma}, \quad \gamma = 3 - D. \quad (25)$$

3 Numerical Analysis

3.1 Initial Conditions

The numerical task consists of finding solutions of the geodesic equation (11) and the equation (19) that enables the calculation of the redshift. Let us call the solution of the former $t(r)$ and the solution of the latter $I(r)$. As we are seeking results along the past light cone, at each step of the independent variable r_i , we need to find t_i first and then use it to find I_i ($i = 1, 2, \dots, n$).

In paper I it was initially proposed to start the integration at $t(0) = 0$ and $I(0) = 0$, but realized that in this approach there would be problems in the elliptic and hyperbolic models because we would get $\frac{0}{0}$ type indeterminations in the function $R(r, t)$ at $r = 0$.

In order to overcome this difficulty I then proposed a flat metric from $r = 0$ till $r = \varepsilon$ (ε small), beyond which the spacetime changed to a curved one. This hypothesis effectively replaces the initial conditions above by $t(\varepsilon) = -\varepsilon$, $I(\varepsilon) = 0$. As we shall see, these new initial conditions produce numerical results which are perfectly acceptable³ and numerically stable, but in this approach the formulation and solution of the interface between flat and curved spacetimes is left incomplete inasmuch as a full determination of this interface demands the solution of the junction conditions between the two regions. If this matching is not fully solved, discontinuities might arise across the joining surface, mainly in the function $R(r, t)$ which determines the luminosity distance. As we are assuming ε small (at least 10^{-3}) these possible discontinuities do not necessarily represent a hazard to the numerical solutions, but we need to have a way to check them.

The match between flat and Tolman metrics is intimately linked to the regularity conditions of the latter and, for the sake of clarity and completeness of this work, I shall discuss briefly the basic argument for Tolman regularity at $r = 0$ (Bonnor 1974), with some additional remarks. Considering a displacement in the 2-surface $t = \text{constant}$, $\phi = \text{constant}$, equation (1) becomes

$$-dS^2 = \frac{R'^2}{f^2} \left(dr^2 + \frac{R^2 f^2}{R'^2} d\theta^2 \right).$$

Near $r = 0$ this 2-surface must be Euclidean, therefore, $R'^2 f^{-2} \rightarrow \text{constant} (\neq 0)$ and

$$\frac{f^2 R^2}{R'^2} \sim r^2,$$

that is,

$$\lim_{r \rightarrow 0} \frac{R'^2 r^2}{f^2 R^2} = 1, \tag{26}$$

which is Bonnor's (1974) equation (2.8). Now, if we suppose that f is approximately constant for small r , equation (26) can be integrated to get $R = r^f$. Therefore,

$$\lim_{r \rightarrow 0} \frac{R'}{f} = \lim_{r \rightarrow 0} r^{f-1}. \tag{27}$$

³ This is especially true as in this problem we are seeking a fractal density profile, and, so, what is relevant to the problem are the intermediary results of the integration and not its final values.

If $f < 1$ the limit above becomes infinity. If $f > 1$ the limit is zero. Hence, $R'f^{-1}$ can only converge to a finite and non-zero constant if $f = 1$ as $r \rightarrow 0$, and $R \sim r$ also near $r = 0$. So the function $f(r)$ as an exponent in equation (27) and with the value $f = 1$ appears to assume a role of *criticality* in regular Tolman solutions.

To calculate the matching between flat and Tolman spacetimes, let us start with two Tolman regions

$$(dS_1)^2 = dt^2 - (R'_1)^2(f_1)^{-2}dr^2 - (R_1)^2d\Omega^2; \quad r < \varepsilon; \quad (28)$$

$$(dS_2)^2 = dt^2 - (R'_2)^2(f_2)^{-2}dr^2 - (R_2)^2d\Omega^2; \quad r > \varepsilon. \quad (29)$$

The Darmois junction conditions at the comoving surface $r = \varepsilon$ were obtained by Bonnor & Chamorro (1990) as

$$R_1(\varepsilon, t) = R_2(\varepsilon, t); \quad f_1(\varepsilon) = f_2(\varepsilon); \quad F_1(\varepsilon) = F_2(\varepsilon). \quad (30)$$

If we take region 1 as flat with static boundary, we can write $R_1 = r$, $f_1 = 1$, and assuming $F_1 = F_2 = F(r)$, provided $F(0) = 0$, the junction conditions (30) are equivalent to

$$R_2[\varepsilon, t(\varepsilon)] = \varepsilon, \quad f_2(\varepsilon) = 1. \quad (31)$$

This result means that on the curved side of the joining surface the solution must be parabolic. Considering the parabolic solution (5) the matching conditions (31) are equivalent to solving the following equation for ε :

$$9F(\varepsilon)[\beta(\varepsilon) - \varepsilon]^2 - 8\varepsilon^3 = 0, \quad F(\varepsilon) \geq 0, \quad (32)$$

where the geodesic for $r \leq \varepsilon$ is the flat one $t = -r$. Therefore, we can start the numerical integration with the initial conditions

$$t(\varepsilon) = -\varepsilon, \quad I(\varepsilon) = 0, \quad (33)$$

while

$$R(\varepsilon) = \varepsilon, \quad R'(\varepsilon) = 1, \quad \dot{R}(\varepsilon) = 0. \quad (34)$$

It was the explicit values of the function $R[r, t(r)]$ on the surface $r = \varepsilon$ that were missing in the previous discussion made in paper I. Notice that the junction conditions do not require R' to be continuous across the joining surface.

It is still possible to simplify the problem by noticing that $\varepsilon = 0$ is actually a solution of equation (32). Hence, instead of initial values (33) and (34) we have

$$t(0) = 0, \quad I(0) = 0, \quad (35)$$

and

$$R(0) = 0, \quad R'(0) = 1, \quad \dot{R}(0) = 0. \quad (36)$$

In this way the previous difficulty of indetermination of the function R at $r = 0$ is avoided as this method allows us to obtain explicit values of R at the origin. This is obviously a consequence of the complete formulation and solution of the interface between the two spacetimes.

The initial conditions (35) and (36) may be obtained alternatively without mention of the flat-curved junction conditions. Around $r = 0$ the regularity conditions $f(0) = 1$, $F(0) = 0$ reduce the field equation (2) to simply $\dot{R} = 0$. As we know that $R \sim r$ when $r \rightarrow 0$, we obtain at once the two other values in equations (36).

In conclusion, we have in practice three sets of initial conditions, where each one, in theory, enables the numerical integration of equations (11) and (19):

- (i) the initial values (33) and (34) with ε being found by solving numerically equation (32);
- (ii) the initial conditions (35) and (36);
- (iii) assuming initial values (33) and taking ε small ($\lesssim 10^{-3}$), but calculating $R(\varepsilon)$, $R'(\varepsilon)$, and $\dot{R}(\varepsilon)$ by putting ε directly into equations (3), (5) and (6) and their derivatives.

This third procedure implies neglecting the results (34) of the matching and that will almost surely give rise to discontinuities in $R(r, t)$. Nevertheless, provided ε is sufficiently small (but not too small otherwise R blows up) and equations (11) and (19) are numerically stable, we would usually get in the end the equivalent results as if we had used initial values (35) and (36) with a small perturbation ε . As we shall see next, this last remark will prove to be most valuable in acquiring confidence in the numerical results.

3.2 Numerical Algorithm

Once the initial value problem for the numerical integration of the first-order ordinary differential equations (11) and (19) is determined, the next step is to choose the numerical integrator that propagates the solution over the interval. In this respect it is essential to bear in mind that what is being sought is a qualitative fractal behaviour for the solutions, that is, solutions which graphically follow the de Vaucouleurs density power law (25). Therefore, high accuracy is not important in this problem. In addition, although the problem is mathematically tricky, the numerical tasks are relatively simple and, so, computational efficiency is of no great concern. In view of this the explicit fourth-order Runge-Kutta method with adaptive stepsize control was the integrator chosen (Press et al. 1986).

As discussed in paper I, the aim of modelling a fractal distribution by Tolman's solution is to make use of the freedom of the arbitrary functions in order to ascertain particular functions $f(r)$, $F(r)$, $\beta(r)$ such that the volume density takes the de Vaucouleurs density power law (25). The way to check whether a fractal distribution was modelled is by taking the logarithm of equation (25)

$$\log \rho_v = a_1 + a_2 \log d_l \quad (37)$$

and finding the constants a_1 and a_2 by linear fitting over the points obtained through numerical integration. The fitting is considered a success if it is linear with a negative slope. That can be concluded by visual inspection of the graph and by an acceptable goodness of fit. Inasmuch as what we are seeking is a qualitative fractal behaviour, very often a visual inspection will be enough.

I shall describe below in general terms the algorithm used to apply the model and obtain the numerical results desired.

- 1) START by choosing special forms for the functions $f(r)$, $F(r)$, $\beta(r)$, such that $f(0) = 1$ and $F(0) = 0$;
- 2) discretize the radial coordinate r_i ($i = 1, 2, \dots, n - 1, n$; $\varepsilon \leq r \leq \Sigma_0$; $r_1 = \varepsilon$, $r_n = \Sigma_0$; total of $n - 1$ steps)⁴;

⁴ In practice the discretization r_i will be performed automatically by the adaptive stepsize control

- 3) make $i = 1$ and choose a set of initial conditions to get t_1 and I_1 ;
- 4) evaluate $f_i, F_i, \beta_i, f'_i, F'_i, \beta'_i$;
- 5) if $f_i^2 > 1$ or $f_i^2 < 1$ then evaluate Θ_i and consider t_i to calculate R_i, R'_i, \dot{R}'_i ; else evaluate directly R_i, R'_i, \dot{R}'_i considering t_i ;
- 6) evaluate $z_i, d_{l_i}, N_{c_i}, V_i, \rho_{v_i}$;
- 7) by using the numerical integrator chosen, advance solution t_{i+1} then use value t_i to advance solution I_{i+1} ;
- 8) make $j = i + 1$ then $i = j$; if $i = n$ then continue below; else return to stage 4;
- 9) make final evaluations f_n, F_n, R_n, R'_n, z_n , etc;
- 10) with the collection of points ρ_{v_k} and d_{l_k} ($k = 2, 3, \dots, n$) perform a $n - 1$ points linear fitting according to equation (37);
- 11) if fitting is unsuccessful then discard used functions $f(r), F(r), \beta(r)$ and go to stage 1; else STOP.

The computer routine which performs this algorithm was written in standard Fortran 77 in double precision and the interested reader can find it in Ribeiro (1992c). Each run of the routine, either successful or not, constituted a different numerical simulation. The program uses many subroutines of Press et al (1986) with some minor modifications. Round-off and truncation errors are monitored at each step by calculating the deviation from zero of the field equation (2) and its first partial derivative in r . Stability and accumulation of errors are monitored by taking the final results as initial conditions to reverse the whole integration and compare the results with the initial values. Error propagation formulas are also used to see whether any of the derived observational quantities acquires unacceptably high errors. The units too are chosen bearing in mind the need to minimize errors and avoid large numbers. Hence, distance is given in Gpc (10^9 pc) and

routine which keeps the accuracy of the numerical results within a desired predetermined value (Press et al. 1986).

in order to have $c = G = 1$, time is expressed in 3.26 Gyr units ($1 \text{ yr} = 3.16 \times 10^7 \text{ s}$) and mass is expressed in units of $2.09 \times 10^{22} M_{\odot}$.

The first numerical simulations used the set (iii) of initial conditions described above with $\varepsilon = 10^{-3}$. The fractional accuracy for the local truncation errors in the variable-step routine was set at 10^{-4} , and this was the value in all simulations, that is, the results throughout this paper were all obtained with this accuracy. This set (iii) of initial conditions applied to equations (11) and (19) led to numerically stable results, with the routine taking a relatively small number of steps to go through the interval of integration. Around 10 to 20 successful steps were usually enough to cover that interval, with 1 or 2 failed steps (see Press et al. 1986, p. 555, for details of the workings of an adaptive stepsize control routine). The reverse integration, that is, taking the final results to integrate backwards in order to compare with the initial conditions, produced a few more failed steps, but the comparison with the initial conditions showed results well within the desired accuracy. These details are important to highlight the smoothness and stability of the solutions, although this approach actually gave rise to discontinuities in R across the surface $r = \varepsilon$, as expected (more details about the way the routine works and its output are available in Ribeiro 1992c).

As far as numerical stability is concerned, the situation changed dramatically when the set (ii) of initial conditions was used, that is, taking $\varepsilon = 0$ and assuming initial values (35) and (36). The solutions became unstable about the origin, with the program being forced to decrease the stepsize so much that it needed to take on the order of hundreds of steps to cover a tiny interval very close to the origin. Once they emerged from this unstable region, the solutions started behaving like the previous approach, covering the remaining region very quickly. The reverse integration behaved likewise, with hundreds of failed steps. Despite this instability the solutions were still very smooth and the comparison of the initial conditions with the results of the backward integration were still well within the desired accuracy. Thus it would appear that with this approach the numerical problem is *stiff* across the joining surface.

Integrating a stiff problem with an explicit Runge-Kutta adaptive stepsize control routine greatly reduces the efficiency of the code as the initial stepsize chosen puts the method at or near numerical instability, which causes a large truncation error estimate.

That leads the routine to reduce substantially the stepsize to keep the local truncation error within the predetermined accuracy. Then the method is able to successfully integrate the problem, but uses a far smaller stepsize and a far greater number of steps than seems justified if we consider the smoothness of the solution (Lambert 1991).

Despite the loss of efficiency, our simulations were usually sufficiently straightforward and computation time did not pose a barrier in most of them. In addition, double precision usually provided enough manoeuvring space for the decrease of stepsize. The situation, however, was far worse when the simulations were carried out using the set *(i)* of initial conditions, that is, with $\varepsilon \neq 0$. The stiffness was so severe that after a few iterations the step length became so small that the difference $r_{i+1} - r_i$ went beyond the machine's precision and the routine achieved an apparently zero stepsize. Obviously such a case cannot be integrated unless an implicit method is used or, perhaps, if a quadruple precision routine is implemented in our explicit Runge-Kutta method. In any case, as the set *(ii)* of initial conditions provides a simpler approach and allows the stiffness to be handled by the program in most cases of interest, these were the conditions used to obtain all results shown in this paper, unless stated otherwise.

It is important to mention that when comparing the results obtained by using the set *(ii)* with the ones produced by the set *(iii)*, the final results of both integrations usually differ by about $|\varepsilon|$, which substantiates the interpretation at the end of §3.1 that the results obtained with initial conditions *(iii)* are usually equivalent to the ones obtained with conditions *(ii)*, but perturbed by about ε (see Ribeiro 1992c for an example of such a situation).

Stiffness is associated with the existence of transient terms in the solution: they contribute very little to the solution, but the usual methods require that they be approximated accurately in order to maintain stability (Gear 1971; Ortega & Poole 1981). In this case it appears that the imposition of the regularity conditions upon the Tolman solution, or the similar process of joining it to a flat region, give rise to these transient terms. Nonetheless, the unanswered question is whether the Tolman stiffness is a mere numerical phenomenon in the solutions, with no major implications, or if it indicates a deeper physical reason in the Tolman models. It is known that some chaotic dynamical systems present stiff behaviour, but the interaction between stiffness and chaos is still

unclear (Cartwright & Piro 1992). More work is necessary in order to clarify this point.

4 The Spatially Homogeneous Special Cases

In this section I shall present the results of the integration of the spatially homogeneous Friedmann models, obtained as special cases of the Tolman metric. The aim of this section is twofold: first to extend the analysis of the Einstein-de Sitter model presented in paper II to the $K = \pm 1$ Friedmann cases, and second to provide numerical results of the Einstein-de Sitter case that can be compared with the exact solution already presented in paper II.

As discussed in §2 the Einstein-de Sitter model is obtained as a special case of the Tolman solution when $f = 1$, $F = \frac{8}{9}r^3$, $\beta = \beta_0$, where β_0 is a constant, and this assumption means that along the past light cone the volume density and luminosity distance are given by (see paper II)

$$\rho_v = \frac{(3\beta_0^{1/3} - r)^6}{54\pi(3\beta_0)^4},$$

$$d_l = \frac{9r\beta_0^{4/3}}{(3\beta_0^{1/3} - r)^2}.$$

Throughout this section I shall assume the value $75 \text{ km s}^{-1} \text{ Mpc}^{-1}$ for the Hubble constant, and this means $\beta_0 = 2.7$ for the Einstein-de Sitter model in our adopted units. Figure 1 shows the $\log \rho_v$ versus $\log d_l$ graph obtained when using the analytical expressions above in the parameter range $0.001 \leq r \leq 1.5$, and figure 2 shows the same results obtained by integrating numerically the Einstein-de Sitter model in the same parameter range. By comparing the two graphs one can see that the numerical integration does reproduce the analytical results. Figures 3 and 4 show respectively the null geodesic $t(r)$ and the function $I(r)$ obtained numerically for this case, and there the smoothness and almost linearity of the solutions within the range of integration are clearly visible. The analytical expressions for these two functions, obtained in paper II, may be written as

$$t = \left(\beta_0^{1/3} - \frac{r}{3} \right)^3 - \beta_0,$$

$$I = 1 - \left(1 - \frac{r}{3\beta_0^{1/3}}\right)^2,$$

and by means of a few direct numerical substitutions one can see that the numerical results shown in figures 3 and 4 do reproduce the analytical functions above, as expected.

The Einstein-de Sitter model also exhibits stiffness, but this is not visible in figure 2 because only steps bigger than 0.0025 were stored in the integration shown in that figure. Figure 5, however, shows the same integration of figure 2, but with all points used by the code being printed. The stiffness is then clearly visible as the program takes an excessive number of steps around $r = 0$ despite the smoothness and linearity of the solutions $t(r)$ and $I(r)$ in the range of the Einstein-de Sitter model shown in figures 3 and 4.

The open Friedmann model with $\Omega_0 \cong 0.2$ is obtained by taking $f = \cosh r$, $F = \sinh^3 r$ and $\beta_0 = 3.6$. Figure 6 shows the numerical results of $\log \rho_v$ against $\log d_l$ for this model, also integrated in the range $0 \leq r \leq 1.5$. By comparing figure 6 with figure 2 we can see that in the open Friedmann model ρ_v departs from a constant value at about $\log d_l = -0.6$ ($d_l \approx 250$ Mpc), while in the Einstein-de Sitter case that happens at about $\log d_l = -1$ ($d_l \approx 100$ Mpc). In other words, the departure from a homogeneous distribution, where ρ_v is constant, is deeper in the open Friedmann model. Stiffness is also present in this case, but in a more severe form as the code took a far greater number of steps for the integration to emerge from around the origin than in the equivalent Einstein-de Sitter integrations.

Finally, figure 7 shows the graph for the recollapsing closed Friedmann model with $\Omega_0 \cong 4$, which is obtained as a special case from the Tolman metric when $f = \cos r$, $F = \sin^3 r$, $\beta_0 = 0.7$. The numerical integrations were also carried out in the same parameter range as the other two cases, and figure 7 shows the results of ρ_v vs. d_l . In this case the volume density starts to change from a constant value at around $\log d_l = -1.5$ ($d_l \approx 30$ Mpc). Therefore, in the recollapsing model the integration along the backward null cone reaches different and earlier spatial sections at closer distances than in the other two spatially homogeneous models. Notice that the values of the luminosity distance where the departure from homogeneity begins are dependent on the Hubble constant used in these integrations, and, therefore, the numbers given above should be

considered as rough approximations.

The recollapsing Friedmann model could not be integrated with the set *(ii)* of initial conditions because the stiffness led to very small first steps, where $F \approx 0$ and $f \approx 1$ when $r \rightarrow 0$. Hence, the two limits of the interval given by equation (8) quickly became extremely big numbers and finding Θ by means of equation (8) broke down due to the machine's precision limitations. Besides, the numerical instability often led to either shell crossing behaviour at very small r or to unacceptably high error accumulation, and in consequence this numerical approach could not be relied upon. As a result the recollapsing integrations were carried out using the set *(iii)* of initial conditions with $\varepsilon = 10^{-3}$.

The results for the $K = \pm 1$ Friedmann cases show that they also do not appear to remain homogeneous along the backward null cone. In addition, considering the form of the graphs of these two cases we can conclude that similarly to the Einstein-de Sitter case studied in paper II, the recollapsing and open Friedmann models do not have single fractal features along the past light cone as they do not follow the de Vaucouleurs' density power law (25). Therefore, considering the IRAS data, all three spatially homogeneous Friedmann models appear to have difficulties in modelling those observations as they predict homogeneity where it is not observed, and for deeper regions all models start to deviate from it.

The apparent inhomogeneity of the Friedmann models is a consequence of the fact that in the present approach densities are expressed along the past light cone, which is where observations are actually made. This means that the volume density ρ_v goes through hypersurfaces of constant t where each one has different values for the proper density. Therefore, although the Friedmann models are *spatially* homogeneous, the volume density will only be homogeneous, that is, have a constant value, in local regions. This will only happen while it is being calculated nearby our present constant time hypersurface, and once we depart from its neighbourhood the volume density starts to change, with the model becoming increasingly apparently inhomogeneous the further the calculations go into the past. The change of the volume density along the geodesic is due to it being a cumulative density, averaging at bigger and bigger volumes in a manner that adds more and more different local densities of each spatial section of the models.

Therefore, under this definition the “homogeneity” of the Friedmann models does not survive. It is important to realize that this interpretation of the “homogeneous” Friedmann model is closely related to the fractal approach to cosmology adopted in this series of papers, inasmuch as the definition for the volume density used here is a direct consequence of the assumption that the large-scale structure of the universe can be described as being a self-similar fractal system.

As final remarks, when one approaches the singularity the model is usually said to become denser because the local density ρ tends to infinity. However, this is *not* the case for the volume density ρ_v , which vanishes at the big bang. This behaviour definitively happens in the Einstein-de Sitter model (see paper II for the asymptotic analysis of this model) and due to the similar form of the graphs of $\log \rho_v$ vs. $\log d_l$ in the open and closed Friedmann models (see figures 6 and 7) as compared to the Einstein-de Sitter case (figures 1 and 2), we can then assume that this vanishing volume density is a feature of all Friedmann models when they approach the singularity. Such a behaviour for ρ_v is, once again, explained by its adopted definition [eq. (23)]: at the big bang singularity hypersurface the observed volume (as defined through the luminosity distance) is infinite, but the total mass within it is finite. It is interesting to note that Wertz (1970) had already postulated a vanishing global density as a requirement for the so-called Pure Hierarchical Models, and similarly Pietronero (1987) conjectured the same sort of result for a fractal distribution. Therefore, it does seem valid to say that at least some aspects of a hierarchical (fractal) cosmology can already be found *within* the standard Friedmannian cosmology, provided one starts with the appropriate definitions.

Empirically, the effect of zero global density in these models as they approach the big bang can be seen as the consequence of the fact that in this work the galaxies one sees empirically on the past light cone are plotted at their luminosity distances, and the luminosity distances go to infinity as z goes to infinity while the number of galaxies remains finite. Observers do often plot their data in ways like that, and an example is Geller & Huchra’s (1989) slices where galaxies are plotted at a distance proportional to their redshift z . If they had extended their plot to z equals infinity only a finite number of galaxies would be inside the horizon and one would see the galaxies thin out to zero. It is obvious, however, that if a different definition of distance had been used (say

comoving distance), this effect of zero global density at the big bang singularity would no longer be necessarily found, nevertheless the redshift or the luminosity distance are observable quantities, independent of cosmology, and observers do use them. Therefore, we can then consider the de Vaucouleurs' density power law as being essentially an empirically observed relation when observables are plotted, and from this perspective this work can be viewed as an attempt to see whether there are any inhomogeneous big bang cosmologies that would allow this empirical relation to be extended to larger scales.

5 Tolman Fractal Solutions

Before discussing the solutions themselves, let us first make some remarks about the three arbitrary functions which may help to simplify the simulations. The function $F(r)$ cannot be a constant, otherwise due to the regularity condition $F(0) = 0$ this constant would have to be zero and there would not be any dust in the model. In addition, due to equation (10) we have to restrict ourselves to $F' \geq 0$, otherwise we would get negative mass in the model. Hence $F(r)$ must be a positive and monotonically increasing function for $r \geq 0$. Notice, however, that there could be ranges for r where $F(r)$ is a nonzero constant and in those ranges $F' = 0$, implying the existence of vacuum regions in the model. The only restriction for the function $\beta(r)$ is that its values must be such that the model is kept within its physical region, that is, such that $t + \beta > 0$. The aim of the simulations is to find a qualitative fractal behaviour which could be expressed in terms of a relatively simple metric. Therefore, it is desirable to obtain fractal behaviour in terms of simple functions. So, wherever possible, I shall restrict the choice of $f(r)$ to the forms it takes in the spatially homogeneous cases, that is, specializing only to $f = \cos r, 1, \cosh r$.

In deciding which solutions are acceptable as fractals, we have the mathematical criterion of verifying whether they follow the equation (25). However, some basic observational constraints must also be obeyed in order to have physically realistic models. The first and most obvious is the observed linearity of the redshift-distance relation for $z \lesssim 1$. The second is the value of the Hubble constant itself which, considering the present uncertainty in its measurements, is accepted to be in the range $40 \text{ km/s/Mpc} <$

$H_0 < 100$ km/s/Mpc (see White 1990 for a recent account on the subject). Finally we have a constraint in the fractal dimension of the distribution. Considering Pietronero's (1987) analysis based on the measurements of the 2-point correlation function, we would have $D \approx 1.4$. However, as other authors claim different and higher values for D (Deng, Wen & Liu 1988; Calzetti & Giavalisco 1991), I shall loosely assume here that the wider range $1 < D < 2$ is reasonable enough for the purposes of this work.

5.1 Parabolic Solutions

The parabolic class of Tolman models is the natural one to start the search for fractal solutions, inasmuch as one of the three functions is already specified, that is, $f = 1$ in this class. Nevertheless, and despite the simplifying remarks above, it was not at all an easy task to find those results. It took over 250 different simulations to find suitable solutions of parabolic type, and one of the major problems was to find the range of the constants in the functions where the overall solution does have a power law behaviour within the interval of integration.

Despite those difficulties, fractal parabolic solutions along the past light cone do exist, although I could only find them by assuming a non-simultaneous big bang, that is, I could not find fractal results with constant $\beta(r)$. Below are the particular forms of the remaining arbitrary functions that led to fractal behaviour in parabolic models:

$$\begin{cases} F = \alpha r^p, \\ \beta = \beta_0 + \eta_0 r^q, \end{cases} \quad (38)$$

and

$$\begin{cases} F = \alpha r^p, \\ \beta = \ln(e^{\beta_0} + \eta_1 r), \end{cases} \quad (39)$$

where α , p , q , β_0 , η_0 , η_1 are positive constants.⁵ The simulations showed that in both cases above α must be around 10^{-4} to 10^{-5} and p and β_0 can vary from around 0.5 to 4. For functions (38) q lies around 0.65 and η_0 around 50. For solutions (39) η_1 varies from about 1000 to 1300. It is difficult to attribute specific roles for each constant as usually

⁵ Actually, by a coordinate transformation F can be made equal to $\frac{8}{9}r^3$, so the only genuine arbitrary function is β .

a change in one of them changes the whole behaviour of the solution, but we can very roughly say that α , q , η_0 and η_1 are more related to the linearity of equation (37) and that p and β_0 are more related to its slope. In other words, changing p and β_0 affects more sharply the fractal dimension of the solutions, but without changing too much their linearity. In addition, if in equations (39) we use instead $\beta = \ln [e^{\beta_0} + \eta_1 (r + r^2)]$, the linearity of the solutions is slightly improved.

Figure 8 presents the results of an integration obtained with functions (38). The fractal dimension is $D = 1.4$ and the integration was carried out in the interval $0 \leq r \leq 2$. In figure 9 one can see the numerical results for the functions (39) integrated in the range $0 \leq r \leq 5$, with the resulting fractal dimension $D = 1.7$. Both figures also show the straight lines fitted according to equation (37) and the qualitative power law nature of the solutions in the integrated interval is visually obvious. We can also see from the figures that the two solutions actually are not much different from one another.

These solutions, however, fail to meet the other observational criteria outlined above. Figure 10 shows the d_l vs. z plot of results of the integrations of functions (38) and the non-linearity of the relation is clearly visible. In addition, the associated Hubble constant is far too low and these reasons seem to rule out as observationally unrealistic a model based on the functions (38). Figure 11 presents the same results for functions (39) and one can see that the redshift-distance relation is mostly linear, especially for the region $z \geq 0.011$. The Hubble constant associated with the linear part of the diagram is around 13, far below the lower limit for H_0 given above, and considering this point it seems that the functions (39) also do not seem to produce a realistic fractal model.

Two remarks must be made about the fractal parabolic solutions above. In the first place, from a mathematical point of view the linearity of the Hubble law ⁶ must be approximately valid through the origin, obeying the equation $d_l = cz/H_0$. This means the redshift distance relation in figure 11 would not be acceptable even though a section of the curve looks linear. However, from a physical viewpoint one might argue that the linearity of the Hubble law is not really needed very near the origin where it would anyway be messed up by local peculiar velocities. In the second place, although it might

⁶ Here by Hubble law I mean the redshift-distance law. See Harrison (1993) for a discussion about the distinction between the Hubble law and the velocity-distance law.

be argued that a different and more observationally acceptable value for the Hubble constant could be obtained by changing the constants until the desired value for H_0 is produced, it must be stressed that the fractal behaviour of the solutions is sensitive (sometimes very sensitive) to the choice of these same constants. In other words, the fractal dimension itself and the limits over which the de Vaucouleurs density power law applies are sensitive to the choice of these constants. Therefore, changing them in order to get a desired value for the Hubble constant will only be successful at the very likely cost of destroying the fractal feature of the solutions over the desired observational range. Due to this reason such a procedure was ruled out in all simulations.⁷

As final remarks, although one cannot say that the functions (38) and (39) are the only ones to produce fractal parabolic solutions as there may be others which lead to fractal behaviour but were not considered here, the experience with all simulations makes it hard to see how other solutions of this kind could be produced in terms of simple functions. This point added to the unrealistic distance-redshift relations of the models leads us to conclude that parabolic type Tolman models do not appear to be able to produce physically realistic fractal models in the backward null cone.

5.2 Elliptic Solutions

The experience with parabolic models was valuable guidance for further studies of Tolman fractal solutions. Elliptic models with power law behaviour in the density were found directly from their parabolic counterparts:

$$\begin{cases} f = \cos r, \\ F = \alpha r^p, \\ \beta = \beta_0 + \eta_0 r^q, \end{cases} \quad (40)$$

and

$$\begin{cases} f = \cos r, \\ F = \alpha r^p, \\ \beta = \ln(e^{\beta_0} + \eta_1 r), \end{cases} \quad (41)$$

⁷ This sensitivity of the fractal solutions to small changes in the constants seems to indicate that the fractal solutions presented in this paper appear to be structurally fragile (Coley & Tavakol 1992).

where $\alpha, p, q, \beta_0, \eta_0, \eta_1$ are positive constants which must lie approximately in the same range as in the parabolic cases in order to produce fractal solutions,⁸ apart from α which must be around the value 10. We have to remember that in the elliptic class models the mass is higher than in the other two classes, which means that the dust does not escape from its own gravitational field and this leads to the eventual halt in the expansion when every part of the model starts to contract. Therefore, it is reasonable to expect a higher value for α in these cases.

The numerical integrations of all elliptic models were carried out using the set (iii) of initial conditions as described in §3.1. This was done for the same reason as in the recollapsing Friedmann model: the set (ii) of initial conditions and equation (8) broke down due to severe numerical instability at very small r , which produced unreliable results, if any.

Figure 12 shows the d_l vs. ρ_v results for functions (40), with a resulting fractal dimension of $D = 1.7$, and figure 13 shows the same results for functions (41) where $D = 2$ was the dimension found. Figure 14 shows the distance-redshift relation for the model with equations (40) and we can see that the plot is not linear. Finally, figure 15 shows the d_l vs. ρ_v plot for the model of equations (41), and although the relation is more or less linear it leads to the low value of roughly 36 for H_0 . Considering all those results together it also seems that equations (40) and (41) produce models which are not compatible with observations. Models with constant β have less linear $\log \rho_v$ vs. $\log d_l$ plots than the two previous ones and lead to too high values for H_0 and D , making them also incompatible with observations.

5.3 Hyperbolic Solutions

The best fractal results in terms of power law behaviour for ρ_v vs. d_l and agreement with observations were obtained by numerical simulations of hyperbolic type solutions. The specializations for $F(r)$ and $\beta(r)$ studied so far also lead to power law behaviour in the density once the function $f(r)$ is modified accordingly. Thus, we have the following

⁸ Since one can make a coordinate transformation in r , only two of the functions f, F, β are really arbitrary.

sets of functions: ⁹

$$\begin{cases} f = \cosh r, \\ F = \alpha r^p, \\ \beta = \beta_0 + \eta_0 r^q, \end{cases} \quad (42)$$

and

$$\begin{cases} f = \cosh r, \\ F = \alpha r^p, \\ \beta = \ln(e^{\beta_0} + \eta_1 r), \end{cases} \quad (43)$$

where, as before, α , p , q , β_0 , η_0 , η_1 are positive constants. In this case the constants will assume approximately the same numerical ranges as in the parabolic case in order to produce fractal solutions, apart from p which for values smaller than 1.4 and greater than 2.5 makes the problem too stiff to be integrated with initial conditions *(ii)*. For those values the use of the initial conditions *(iii)* will produce the desired results.

Figure 16 shows the ρ_v vs. d_l numerical results of the integration of the model using equations (42) and the fitted straight line, which leads to a fractal dimension $D = 1.4$, while figure 17 shows the redshift-distance diagram. Although the latter relation is approximately linear, it leads to an $H_0 \approx 23$ km/s/Mpc, a value too low to make equations (42) a model compatible with observations.

The power law behaviour, leading to fractal dimension $D = 1.3$, of the results of the numerical integrations of the model formed by functions (43) can be seen in figure 18. Figure 19 shows the redshift-distance diagram of the same model and we can see that the plot is linearly well approximated. More important, a simple calculation shows that the slope of the approximated line formed by the points in figure 19 gives $H_0 \cong 61$ km/s/Mpc. Therefore, the model formed by functions (43) is the first so far to reasonably agree with all basic requirements outlined above in order to make the model compatible with current observations: linearity of the d_l vs. z diagram, Hubble constant within the currently accepted uncertainty, power law behaviour for the ρ_v vs. d_l results and fractal dimension around the values which are in agreement with present calculations of the 2-point correlation function. Note incidentally, that the integrations were stopped

⁹ As in the elliptic case, here again only two functions are really arbitrary.

at $d_l \cong 350$ Mpc, which corresponds to $z \cong 0.07$, as this is the redshift of the deepest self-similar structures identified in the IRAS survey (Saunders et al. 1991).

Even better results were obtained with the mathematically and physically simpler model below:

$$\left\{ \begin{array}{l} f = \cosh r, \\ F = \alpha r^p, \\ \beta = \beta_0. \end{array} \right. \quad (44)$$

This is obviously a simultaneous big bang model, like its Friedmann counterpart, and is physically and mathematically the closest model to the open Friedmann one, differing only in the function $F(r)$ which gives the distribution of dust. Figure 20 shows the power law behaviour of ρ_v vs. d_l of the model formed by functions (44), with a fractal dimension of $D = 1.4$. Figure 21 is the redshift-distance diagram of the same model where we can see the good linear approximation given by functions (44). The slope of the points gives $H_0 \cong 80$ km/s/Mpc, and it is interesting to note that recent measurements made by two different methods suggest a Hubble constant very close to this value (Peacock 1991). Actually, for $\beta_0 = 3.6$, the value used to get the results shown in figures 20 and 21, we would have an age of the universe of about 12 Gyr, which is a lower limit if we consider the age of globular clusters (Peacock 1991). Therefore, also in this point of the age of the universe the model (44) agrees reasonably well with observations. The integrations with functions (44) were also stopped at $z \cong 0.07$, which in this case corresponds to the luminosity distance $d_l \cong 270$ Mpc. Finally, figure 22 shows the results for cumulative number counting vs. redshift produced by the model under consideration.

6 Discussion

6.1 A Metric for a Smoothed-out and Averaged Fractal

In the previous section it was shown that Tolman fractal solutions do exist, and that the only ones compatible with observations are the hyperbolic type solutions obtained by means of the specializations given by equations (43) and (44).¹⁰ As in equations (43) the

¹⁰ Notice however that fractal solutions of elliptic and parabolic types may, in principle, be obtained from other more complex specializations of the arbitrary functions than the ones considered in this

function $\beta(r)$ is not constant, this means that the model has no simultaneous big bang. In other words, in a model of this sort the big bang singularity hypersurface occurred at different proper times in different locations, and the age of the universe is different for different observers at different radial coordinates. More specifically, as $\beta(r)$ in equations (43) is an increasing function, regions at smaller r are younger than at bigger r , and the youngest region of the model is “here”, at $r = 0$.

An universe model where some regions are older than others is not as odd in terms of accepted ideas of galaxy formation as it might seem at first. Inasmuch as the observed universe is lumpy, in a spatially homogeneous Friedmann universe where $\rho = \rho(t)$ and the big bang singularity is simultaneous, there must be density fluctuations $\delta\rho/\rho$ of some kind in order to form galaxies, and it is necessary to have some sort of metric perturbations for that to happen. So, at the era of galaxy formation, which may be defined as a hypersurface of constant time in order to agree with our intuition in an unperturbed metric, in the perturbed metric the overdensities ρ_o occur at time t_o and the underdensities ρ_u occur at t_u , and t_o must be different from t_u , otherwise there would not be any fluctuation at all. In other words, due to the density fluctuations $\delta\rho/\rho$, in the perturbed metric a hypersurface of constant density no longer coincides with a hypersurface of constant time. Therefore, a deviation of the Friedmann metric from spatial homogeneity, even if it is small, is essential for lumpiness and, hence, some regions will inevitably have different local times than others. In the perturbed metric we may even define the era of galaxy formation as being a hypersurface of constant density. In other words, a non-simultaneous big bang seems inevitable in order to form galaxies in the standard scenario, even if those differences in local times are small.

Note that this discussion assumes that a hypersurface of simultaneity is defined by a specific value of the proper time, which is a logical thing to do in an unperturbed metric. In a perturbed metric, however, one could define the hypersurfaces of simultaneity in a different way, which would mean a different choice of gauge by which the perturbed and the non-perturbed spacetimes are related.

Nevertheless, considering it is desirable that fractal models be as close as possible to their Friedmann counterparts, and also considering mathematical simplicity, I shall

paper, and these solutions could be compatible with observations.

take the specializations given by equations (44) as the best modelling of a relativistic hierarchical (fractal) cosmology by Tolman's spacetime. Let us now write this model explicitly. Its metric is expressed as

$$dS^2 = dt^2 - \left(\frac{R'^2}{\cosh^2 r} \right) dr^2 - R^2(d\theta^2 + \sin^2 \theta d\phi^2); \quad r \geq 0, \quad R[r, t(r)] \geq 0. \quad (45)$$

The Einstein field equation for this metric may be written as an energy equation (Bondi 1947; paper I)

$$\frac{\dot{R}^2}{2} - U(R) = E(r), \quad (46)$$

where

$$U(R) = \frac{\alpha r^p}{4R} \quad (47)$$

is the effective potential energy, and

$$E(r) = \frac{1}{2} \sinh^2 r \quad (48)$$

is the total energy within r . The solution of equation (46) is

$$R = \frac{\alpha r^p}{8E(r)} (\cosh 2\Theta - 1), \quad (49)$$

where Θ is given by

$$4[t(r) + \beta_0] [2E(r)]^{3/2} = \alpha r^p (\sinh 2\Theta - 2\Theta), \quad (50)$$

$t(r)$ is the solution of the past radial null geodesic

$$\frac{dt}{dr} = -\frac{R'}{\cosh r}, \quad (51)$$

and the local density is expressed as

$$\rho = \frac{4p[E(r)]^2}{\pi \alpha r^{p+1} R' (\cosh 2\Theta - 1)^2}. \quad (52)$$

The essentially new physical feature of the model above is its single difference from the open Friedmann one: the form of the function for the gravitational mass. That is given by $F = \alpha r^p$, while in Friedmann this function must be $F = b_2 \sinh^3 r$. Remembering that $\alpha = 10^{-4} - 10^{-5}$ and $p = 1 - 2.5$, the fractal metric (45) appears to have a more rarefied dust than its Friedmann equivalent. As fractal models are characterized by a power law nature of their average densities, with fractional exponents smaller than 3, it is hardly surprising that such models have a more rarefied distribution of mass.

6.2 Evolution of the Fractal Model and Comparison with the Spatially Homogeneous Case

The constant β_0 in equation (50) gives the universal big bang time if we define “now” as $t = 0$, and this fact allows us to study the evolution of the fractal model (45) through the easily computable manner of simply varying β_0 . This investigation permits us to answer the question of whether or not the fractal features of the metric (45) are present at different epochs. Bearing this point in mind, I carried out simulations for different values of β_0 in the interval $0 \leq r \leq 0.07$, but keeping $\alpha = 10^{-4}$ and $p = 1.4$ in all of them. I found out that the model under consideration remains fractal in integrations where $\beta_0 = 1.5, 2, 2.5, 3.6, 4.5$ and 6 , with the resulting fractal dimensions being $D = 1.5, 1.5, 1.5, 1.4, 1.4$ and 1.4 , respectively. These results show that the metric (45) effectively models a fractal distribution of dust at different epochs, with a remarkable constancy in D . All those integrations had $r = 0.07$, the final value of the integrating parameter, corresponding to $z \cong 0.07$, although the luminosity distance varied from $d_l \cong 110$ Mpc when $\beta_0 = 1.5$ to $d_l \cong 450$ Mpc when $\beta_0 = 6$. This variation may be physically explained as due to changes in the Hubble constant itself, whose values get bigger at earlier epochs. Finally, those results together with some simulations on different values of p suggest it is possible to propose a simple, but very restricted, relationship between p and D . For $0 \leq r \leq 0.07, 1.5 \leq \beta_0 \leq 6$ and $1.4 \leq p \leq 2.5$ we can say approximately that $D = p \pm 0.1$.

An interesting question about the model (45) is to see how it would compare with the spatially homogeneous open Friedmann one. Looking at the results of the latter in figure 6 and the former in figure 20 we can qualitatively see that the absolute value of the difference in $\log \rho_v$ between the two models starts as zero, but increases rapidly. In the analytical study of the Einstein-de Sitter model presented in paper II it was shown that at the big bang singularity hypersurface the volume density ρ_v vanishes and the luminosity distance d_l goes to infinity, and this effect is a consequence of the definition (23) of the volume density: at the big bang the volume (22) is infinity, but the total mass is finite. As already said at the end of §4, we can therefore expect a similar asymptotic effect in both the open Friedmann case and the fractal model (45), and this means that the difference in ρ_v between these two models should start decreasing after reaching a maximum in its increase. Actually, figure 6 already shows a sharp decrease of ρ_v in

the open Friedmann case, but as the integrations of the model (45) in figure 20 did not go far enough in the past, the results cannot show where this maximum might be. Nevertheless, based on this reasoning we can deduce that the observational relations of the fractal model (45) appear to be asymptotically Friedmann when calculated along the past light cone.

6.3 Relations to Homothetic Self-Similarity

Another topic which deserves some investigation is the relation, if any, between self-similarity due to fractals and self-similarity due to homothetic Killing vectors (Cahill & Taub 1971). There is some interest in this point because some attempts have been made to explain large-scale voids and clusters by self-similar perturbations of a Friedmann universe (Carr & Yahil 1990), and also because the first attempt to propose a workable relativistic hierarchical cosmology was done assuming a homothetic self-similar metric (Wesson 1978, 1979).

In general relativity a spacetime is called self-similar if all metric components can be put in a form in which they are functions of a single independent dimensionless variable which is a combination of the spacetime coordinates. Mathematically, this corresponds to the existence of homothetic Killing vectors, meaning that spherically symmetric similarity solutions are unchanged by coordinate transformations of the form $t \rightarrow bt$, $r \rightarrow br$, for any constant b obeying the conformal transformation $g_{\mu\nu}(r, t) \rightarrow \frac{1}{b^2}g_{\mu\nu}(r, t)$ (Cahill & Taub 1971). Physically, spherically symmetric similarity spacetimes with $\Lambda = 0$ contain no fundamental scales or dimensional constraints (Henriksen & Wesson 1978), and it would seem that these features make homothetic self-similarity a possible mathematical version of the scaling idea behind the empirical hierarchical clustering concept. However, homotheties, as defined in general relativity, are basically geometrical features which will not necessarily translate themselves in observable quantities. In other words, the geometrical scaling features of the model do not necessarily mean that its observational relations are also scaling. For this reason it seems that homothetic self-similarity provides an unsatisfactory manner of modelling hierarchy.

It is beyond the aims of this work to make a general discussion about the possible relations between these two types of self-similarity. However it is of interest to investigate

whether or not the fractal solutions presented in §5 are homothetic. Recently Lemos & Lynden-Bell (1989) and Ponce de Leon (1991) studied homotheties in Tolman models and found that specific criteria are necessary to maintain the assumed similarity symmetry in the solutions. For models where $\Lambda = 0$ (our case here), they showed that the first criterion is for the function $f(r)$ to be constant, that is, each comoving shell must have the same total energy. That immediately tells us that all fractal solutions of elliptic and hyperbolic type studied here, including the metric (45), are not homothetic, leaving only the parabolic solutions still to investigate. The next criterion says that homothetic solutions with $f(r) = 1$ restrict the mass distribution to have the form $F(r) = \text{constant} \times r^{2\varphi+3}$, where φ is a constant, and this is the case in the solutions (38) and (39). The final requirement for homothetic symmetry to hold in our Tolman solutions demands that for $f = 1$ and $\varphi \neq 0$ the big bang hypersurface must be of the form $\beta(r) = a + br^{-\varphi}$, where a and b are constants. The solution (38) satisfies these three requirements only if $p = 3 - 2q$. The solution (39) can have $\beta(r)$ reduced to its form in equations (38), but then the value $p = 1$ must hold to satisfy the third requirement. Therefore, very restricted cases of the fractal solutions (38) and (39) have also homothetic self-similarity.

In conclusion, from what we have seen it does appear valid to say that fractal self-similarity is a much weaker requirement on the solutions than homotheties, and although we have reached this conclusion looking in more detail only at the Tolman spacetime, based on the self-similar requirements for both cases it seems reasonable to suppose that this conclusion may well be valid in general.

6.4 Fitting Condition

In the previous section of this paper we dealt with the problem of finding a specific Tolman model which best represents the observed inhomogeneous distribution of galaxies, and in that respect it was concluded that the metric (45) is the simplest one to achieve this aim. In other words, what was being sought was the optimal way of fitting the Tolman metric to the real lumpy large-scale structure of the universe. It was discussed in paper I that it may be desirable for us to have a Friedmann metric as background spacetime to the inhomogeneous Tolman region (or regions) used here to describe a fractal distribution of galaxies, and having found the specific forms for this inhomogeneous

region an important question arises at once: what are the implications that the fractal metric (45) and the hyperbolic solution (43) bring to a possible Friedmann spacetime background? Answering this question is equivalent to finding a response to the “fitting problem” in cosmology, in the specific context of this work.

Ellis & Stoeger (1987) have outlined the fitting problem as being the search for an ideal Friedmann model which best fits another cosmological model that gives a realistic representation of the universe, including all inhomogeneities down to some specified length scale. In Ellis & Stoeger’s words, “the approach resembles that used in geodesy, where a perfect sphere is fitted to the pear-shaped earth; deviations of the real earth from the idealised model can then be measured and characterized”. Various ways in which this approach might be tried are discussed in detail by them, however here we shall restrict ourselves to the specific one outlined by Ellis & Jaklitsch (1989) where the matching between the Tolman and Friedmann spacetimes is interpreted as a fitting condition.

It was shown in paper I that the Darmois junction conditions between the two spacetimes under consideration require that $f = g'$ on the joining surface. Here $g = \sin r$, r , $\sinh r$ is the function which determines the curvature of the Friedmann model. As both the solution (43) and the metric (45) are of hyperbolic type with $f = \cosh r$, there is no way of satisfying this condition when $r > 0$ unless we have $g = \sinh r$. Therefore, the first response to the fitting problem in this context says that our Tolman fractal solutions imply an open Friedmann background model.

It was also shown in paper I that the matching between these two spacetimes severely restricts the gravitational mass inside the Tolman cavity. If $m(r) = F(r)/4$ is the gravitational mass of the Tolman region within a comoving radius r , and $\bar{m}(x) = 4\pi\mu a^3(t)g^3(x)/3$ is its Friedmann equivalent for a radius x and dust density μ , the junction conditions demand

$$m(\Sigma_0) = \bar{m}(\Sigma_0), \tag{53}$$

where Σ_0 is the constant that defines the joining surface $r = x = \Sigma_0$ between the two spacetimes. Therefore, as discussed by Ellis & Jaklitsch (1989), equation (53) allows us to choose the Friedmann background model whose density is appropriate to our lumpy Tolman model. Let us see in more detail how this background spacetime can be specified.

In the open Friedmann model the local density is given by

$$\mu = \frac{3b_2}{16\pi a^3(t)},$$

and as $F = \alpha r^p$ in our fractal models, we can then write the equation (53) as

$$\alpha \Sigma_0^p = b_2 \sinh^3 \Sigma_0. \quad (54)$$

The value of the parameter b_2 is what we are seeking in order to determine precisely the Friedmann background and give a more accurate answer to the fitting problem in this context. Equation (54) shows that b_2 is dependent on the other three parameters α , p , Σ_0 , and hence, there is a certain degree of flexibility in choosing the mass of the background spacetime. Thus, even when the interior region is determined by known values of α and p , different values of b_2 are obtained according to exactly where the joining surface is located.

We can work out how the Friedmann background is in the case of the numerical integrations of the model (44) shown in figure 20. We have $\alpha = 10^{-4}$, $p = 1.4$, and if we take $\Sigma_0 = 0.07$ (the value where the numerical evaluation ends) we get $b_2 = 0.007$, $\Omega_0 \cong 0.002$ and $H_0 = 83$ km/s/Mpc. This low value for Ω_0 is in the lower limits of the interval where it has been reportedly measured. However, it is important to notice that in the approach used in this work no kind of dark matter was considered, but only the luminous matter associated with galaxies. Galactic luminous matter gives a value for Ω_0 of the same order of magnitude as the one found for the background model above (see White 1990, p. 38).

As a final remark, we have so far considered the interior Tolman region joining directly to the exterior Friedmann metric. That does not need to be always the case and we can envisage an interior region surrounded by one or more intermediary regions with higher or lower densities, in a scheme designed to model specific observational features. For example, a structure like the ‘‘Great Wall’’ (Geller & Huchra 1989; Ramella, Geller & Huchra 1992) could be modelled by an intermediary overdensity region before the background spacetime is reached, and with an underdensity interior fractal Tolman region (see Bonnor & Chamorro 1991 on how to join an underdensity Tolman region to an overdensity intermediary section). Such a modelling will obviously increase the value of

Ω_0 for the fitted Friedmann background. This method, however, demands more detailed work in order to achieve a model where this sort of structure is precisely characterized. I shall not pursue further this study here.

6.5 Criticism of Criticisms of Fractal Cosmology

As the final issue of this section, I shall discuss some of the objections raised by some authors against a fractal cosmology. The first type of criticism is contrary to a possible unlimited fractal pattern for the large-scale clustering of galaxies, and although some of the critical voices do accept fractals at small scales, their objections are usually based either on reasoning from the 2-point angular correlation function (Peebles 1989), or on supposed strong theoretical limitations of the standard Friedmannian cosmology. Therefore, in one way or another those authors see the strong need for a crossover to homogeneity on the fractal structure, at a scale yet to be agreed upon.

Criticisms based on the angular correlation function have been addressed by Coleman & Pietronero (1992) and I shall not discuss them here, although this point was briefly mentioned in paper II. The theoretical criticisms, on the other hand, must be addressed in this paper, and for this purpose I shall reproduce here two quotations from Martínez (1991) which well represent this point of view, although he is by no means the only one to raise such kind of objections. Martínez states that “... it should be noted that in the standard cosmology, the distribution of mass must tend to a non-zero finite density when averaged over large volumes”¹¹. From a relativistic point of view, the problem with this statement is its failure to specify where this average is supposed to be carried out. It is correct to say that if in a Friedmannian cosmology we make averages of density at spacelike hypersurfaces of constant t , those averages cannot be zero as this cosmology is spatially homogeneous. However, at large volumes such averages would be observationally irrelevant as astronomy in the electromagnetic spectrum is actually made along the backward null cone and *not* at such spacelike hypersurfaces. Therefore,

¹¹ The expression “large volumes” used in this quotation is imprecise, and can be interpreted as meaning either big local volumes or volumes which are big enough to be no longer considered as local. In a cosmological context the latter is more appropriate and from now on I shall assume the expression “large volumes” to mean non-local ones.

the statement above is only true in an unobservable situation, and considering that voids and clusters of galaxies were, and still are being, identified in the so-called redshift space, which lies on the past null cone, this is where the average of density must be carried out. Hence, the quotation above is inappropriate as an objection to a fractal structure for the distribution of galaxies. These two types of averages will only coincide locally, and it will depend on the model and the value assumed for the Hubble constant in order to establish what scales are local, although, in any case they will certainly differ at large volumes. In effect, in this imprecise formulation this statement may actually reinforce, or be taken by, a common misinterpretation of the standard model, which, due to inappropriate Newtonian analogies, confuses the model's geometry with its observable quantities .

Martínez (1991) goes on and states that "... a fractal universe without a crossover to homogeneity (...) implies a vanishing density for very large volumes and this idea cannot be accepted without creating important additional problems". It was shown in paper II (and rediscussed in §4) that if averages on density are made along the backward null cone, at the big bang singularity hypersurface the luminosity distance goes infinite and this average density is zero. That happens in the Einstein-de Sitter model, the most popular of the cosmological models, and no additional hypothesis or change in the metric was done to achieve this result. The point is, once more, where the average is made and which definition of density is adopted. Thus, again the statement is in fact an untenable objection since the standard cosmology does have a vanishing average density without any important additional problem. Having or not having zero average density in the model is just a question of interpretation.

It should be clearly understood that the above criticisms of Martínez's (1991) statements are made solely on the grounds of the standard Friedmannian cosmology, and there is no need whatsoever to mention any fractal hypothesis in order to show the impreciseness and inappropriateness of such statements. The important point being that even accepting the spatially homogeneous standard Friedmannian cosmology, this model tells us we would only be able to see, through our telescopes, its homogeneity locally.

Closely related to this point of local homogeneity is the issue, one could argue, of how we would understand in this context the reported uniform distribution of some

deep samples like radio sources. In the first place it must be made very clear that the discussion made so far is aimed at showing that from a theoretical point of view there is no constraint to an unlimited fractal distribution, even from within a Friedmannian framework, but that does not imply the fractal system is indeed limitless, as an upper cutoff to homogeneity is not yet ruled out.¹² Nonetheless, a simple calculation in the Einstein-de Sitter model, as presented in paper II, will show that a 30% decrease in ρ_v (from the value at present time $t = 0$) occurs at $z \approx 0.1$ ($d_l \approx 500$ Mpc), and this means that even considering such high error in the determination of the volume density, this is, roughly speaking, the maximum approximate range where the homogeneity of this model could be observed. Beyond this range the homogeneity of the Einstein-de Sitter model would no longer be observed in the past light cone. Thus the first issue raised by this result is a problem of methodology: curvature effects occur in Friedmann models at much closer ranges than usually assumed, and this means that those surveys must consider in their data analysis expressions along the past light cone. Currently, calculations of observational relations where the backward null cone is taken into account is a very much neglected problem in cosmology. Secondly, if it is confirmed that in those deep surveys the distribution is really uniform, that would put the Friedmann model in even greater difficulties as it would appear to predict inhomogeneity in deeper ranges where this would not be observed. Thirdly, the sceptical viewpoint on this issue would be to argue that usually deeper observations are less precise than shallower ones, and previous claims of the so-called homogeneous “fair-sample” finally being observed did not stand once more refined and complete observations were made. Historically, the range at where the homogeneity is, or would be, finally reached has being pushed further and further away as more complete data become available and observational techniques improve, and so, the sceptic may say, we may not have necessarily seen the end of this story.

In addition to the points discussed above, a second kind of criticism to the fractal cosmology has been voiced by Peebles, Schramm, Turner & Kron (1991) in the following

¹² The proposal for an upper cutoff to homogeneity in the fractal system appears to have been initially advanced by Ruffini, Song & Taraglio (1988), although Pietronero (1987) had already made a discussion about this issue.

form. “If the galaxy distribution had been observed to follow a pure scale-invariant fractal, (...) the closely thermal spectrum and isotropy of the cosmic background radiation in this highly inhomogeneous Universe would have been a deep puzzle”. First of all, it should be said that in an inhomogeneous model with a Friedmann background, the apparent discrepancy between the inhomogeneity of the model and the isotropy of the microwave background is not really an issue as the junction conditions already require that an overdensity must be compensated by an underdensity before the uniform region is reached, in order that the average densities will be the same (see paper I, §4). Nevertheless, the most important point is the result already obtained in paper II and extended in this paper for the other Friedmann models: the standard Friedmannian cosmology may be taken to be inhomogeneous depending on how we look at it. That means that the apparent contradiction between inhomogeneity and the isotropy of the microwave background may not be a contradiction at all. This is an essential point in order to put Peebles, Schramm, Turner & Kron’s statement above into perspective, as we have already seen in this paper and in paper II that at relatively modest luminosity distances and redshifts, even the standard spatially homogeneous Friedmannian cosmology becomes highly inhomogeneous on the past light cone because ρ_v departs considerably from its constant value in our constant time hypersurface the further into the past we look, and ρ is dependent on r . Considering that so far even the deepest all-sky redshift surveys have failed to reach the so-called “fair sample” where the homogeneity is supposed to be, waiting for us to discover it, perhaps it is about time to ask if the cosmic background radiation could be accommodated in a different cosmology, or wonder whether it is really a deep puzzle.

After all this discussion, we are left with an important point to consider. If the supposed theoretical need for a crossover to homogeneity in the fractal system is much weaker than previously thought, we have the question: is it really necessary? Since we have seen here and in paper II that even the Friedmann models do not seem to remain homogeneous along the past null geodesic (see figures 1, 2, 6 and 7), if the homogeneity of the standard model does not survive, where is the strong need for a crossover? In paper I it was assumed that the Tolman metric would eventually join a Friedmann background and, among other things, I argued the need for that was to

make the model compatible with a different interpretation of the Copernican principle. However, in the light of inhomogeneity even in the Friedmann metric, it could be argued that from an observational point of view, that is, in calculations along our past null cone, if the relativistic fractal cosmology developed in this series of papers has or has not a Friedmann background might well be irrelevant.

7 Conclusion

In this work I have presented numerical solutions of particular Tolman models of elliptic, parabolic and hyperbolic types featuring fractal behaviour along the past light cone. The initial conditions of the numerical problem is discussed in detail and I found three different sets of initial values that can, in principle, be used to solve the problem numerically. In practice, however, I have made use of only two due to strong stiff behaviour in the numerical solutions. The algorithm used to get the solutions has been described, as well as some details of the manner it was implemented in the computing code.

The spatially homogeneous Friedmann models were treated as special cases of the Tolman solution and solved numerically. In an extension of the results of paper II, I have found that the $K = \pm 1$ Friedmann cases also do not appear to remain homogeneous along the backward null cone, and this is explained because the models are *spatially* homogeneous: when the density is averaged along the null geodesic, going through hypersurfaces of constant t , but with different values for the local density, this average changes. Furthermore, as in the open and closed Friedmann models the volume density decreases the farther we go, it would seem that similarly to the Einstein-de Sitter model studied in paper II, all cases of the standard cosmological model have *zero* global density at the big bang singularity hypersurface.

Fractal solutions were obtained in all classes of Tolman's solution and the mathematical criterion for getting them was their obedience to the de Vaucouleurs' density power law. Nonetheless, considering that observationally realistic models have to follow the linearity of the luminosity distance–redshift diagram, have a Hubble constant within the currently accepted uncertainty and fractal dimension in agreement with measurements of the 2-point correlation function, I found only hyperbolic type solutions obeying all

these criteria.

The simplest fractal hyperbolic solution has simultaneous big bang and it was found that this model has fractal features in many different epochs, does not have homothetic self-similarity (although some of the parabolic fractal solutions do) and if we assume a Friedmann background spacetime, the matching between these two metrics imply that the background must be an open Friedmann model. A different scenario where the “Great Wall” could be modelled was also considered. The paper ends with a discussion on some objections raised by some authors against a fractal cosmology, where I have shown how some are imprecise and inappropriate, leading to untenable objections to this sort of cosmology.

And what about the origin of this fractal system? If a Friedmann background is assumed, it might be a cellular-type structure (Feng, Mo & Ruffini 1991; Fabbri & Ruffini 1992 and references therein), but with the difference that an upper cutoff to homogeneity in the past light cone is not compulsory, as discussed in the previous section. In this case this structure could be a result of a fragmentation process (Ruffini, Song & Taraglio 1988). If we do not assume a Friedmann background, Bonnor (1974) showed that a hyperbolic Tolman model can start inhomogeneous, remain inhomogeneous during the course of its evolution and at large times, when the dust has already escaped from its own gravitational field, there is nothing that could alter the model’s density distribution. In this case the function $\beta(r)$ does not appear neither in the function $R(r, t)$ nor in the density ρ , which was interpreted as meaning that at large t the model has “forgotten” its big bang, at least as far as the density is concerned. In conclusion, the origin of the fractal structure appears to be an open problem.

Acknowledgements

I thank M. A. H. MacCallum for his guidance during this research and for valuable suggestions and discussions in all stages of this work. I am also grateful to W. B. Bonnor for discussions and suggestions, J. H. E. Cartwright for discussions about stiff problems

and T. Allen, A. B. Burd and J. E. F. Skea for suggestions on numerical integrations. Finally I thank W. Seixas for his help with computing problems and A. Koutras for discussions on homotheties. This work had the financial support of the Brazilian Agency CAPES.

References

- Bondi, H. 1947, *M. N. R. A. S.*, 107, 410.
- Bonnor, W. B. 1974, *M. N. R. A. S.*, 167, 55.
- Bonnor, W. B. & Chamorro, A. 1990, *Ap. J.*, 361, 21.
- Bonnor, W. B. & Chamorro, A. 1991, *Ap. J.*, 378, 461.
- Cahill, A. H. & Taub, M. E. 1971, *Commun. Math. Phys.*, 21, 1.
- Calzetti, D. & Giavalisco, M. 1991, in *Applying Fractals in Astronomy*, ed. A. Heck & J. M. Perdang, p. 119 (Springer-Verlag: Berlin).
- Carr, B. J. & Yahil, A. 1990, *Ap. J.*, 360, 330.
- Cartwright, J. H. E. & Piro, O. 1992, *Int. J. Bifurcation and Chaos*, in press.
- Coleman, P. H. & Pietronero, L. 1992, *Phys. Reports*, 213, 311.
- Coley, A. A. & Tavakol, R. K. 1992, *Gen. Rel. Grav.*, 24, 835.
- Deng, Z.-G., Wen, Z., & Liu, Y.-Z. 1988, in *Large Scale Structures of the Universe*, Proc. of the 130th IAU Symposium, ed. J. Audouze, M.-C. Pelletan & A. Szalay, p. 555 (Kluwer Academic Publishers: Dordrecht).
- Ellis, G. F. R. & Stoeger, W. 1987, *Class. Quantum Grav.*, 4, 1697.
- Ellis, G. F. R. & Jaklitsch, M. J. 1989, *Ap. J.*, 346, 601.
- Fabbri, R. & Ruffini, R. 1992, *Astron. Astrophys.*, 254, 7.

- Feng, L. L., Mo, H. J. & Ruffini, R. 1991, *Astron. Astrophys.*, 243, 283.
- Gear, C. W. 1971, *Numerical Initial Value Problems in Ordinary Differential Equations* (Prentice-Hall: Englewood Cliffs).
- Geller, M. J. & Huchra, J. P. 1989, *Science*, 246, 897.
- Harrison, E. 1993, *Ap. J.*, 403, 28.
- Henriksen, R. N. & Wesson, P. S. 1978, *Ap. Space Sci.*, 53, 429.
- Lambert, J. D. 1991, *Numerical Methods for Ordinary Differential Systems* (John Wiley & Sons: Chichester).
- de Lapparent, V., Geller, M. J. & Huchra, J. P. 1986, *Ap. J. (Letters)*, 302, L1.
- Lemos, J. P. S. & Lynden-Bell, D. 1989, *M. N. R. A. S.*, 240, 317.
- Martínez, V. J. 1991, in *Applying Fractals in Astronomy*, ed. A. Heck & J. M. Perdan, p. 135 (Springer-Verlag: Berlin).
- Ortega, J. M. & Poole, W. G., Jr. 1981, *An Introduction to Numerical Methods for Differential Equations* (Pitman: Marshfield).
- Peacock, J. 1991, *Nature*, 352, 378.
- Peebles, P. J. E. 1989, *Physica D*, 38, 273.
- Peebles, P. J. E., Schramm, D. N., Turner, E. L. & Kron, R. G. 1991, *Nature*, 352, 769.
- Pietronero, L. 1987, *Physica*, 144A, 257.
- Ponce de Leon, J. 1991, *M. N. R. A. S.*, 250, 69.
- Press, W. H., Flannery, B. P., Teukolsky, S. A. & Vetterling, W. T. 1986, *Numerical Recipes: The Art of Scientific Computing* (Cambridge: Cambridge).
- Ramella, M., Geller, M. J. & Huchra, J. P. 1992, *Ap. J.*, 384, 396.

- Ribeiro, M. B. 1992a, Ap. J., 388, 1 (paper I).
- Ribeiro, M. B. 1992b, Ap. J., 395, 29 (paper II).
- Ribeiro, M. B. 1992c, Ph.D. thesis, Queen Mary & Westfield College - University of London.
- Ruffini, R., Song, D. J. & Taraglio, S. 1988, Astron. Astrophys., 190, 1.
- Saunders, W., et al. 1991, Nature, 349, 32.
- Tolman, R. C. 1934, Proc. Nat. Acad. Sci. (Wash.), 20, 169.
- Wertz, J. R. 1970, Ph.D. thesis, University of Texas at Austin.
- Wesson, P. S. 1978, Ap. Space Sci., 54, 489.
- Wesson, P. S. 1979, Ap. J., 228, 647.
- White, S. D. M. 1990, Physical Cosmology, in Physics of the Early Universe, ed. J. A. Peacock, A. F. Heavens & A. T. Davies, p. 1 (Edinburgh University Press: Edinburgh).

Figure Captions

- Figure 1: This graph is the same appearing in paper II and shows the analytical results of a $\log \rho_v$ vs. $\log d_l$ plot for the Einstein-de Sitter model in the range $0.001 \leq r \leq 1.5$ and with $\beta_0 = 2.7$. The inhomogeneity of the model along the past null geodesic is clearly visible.
- Figure 2: Plot of the numerical results of the volume density ρ_v against the luminosity distance d_l in the range $0 \leq r \leq 1.5$ for the Einstein-de Sitter model. Only steps bigger than 0.0025 are shown here. Distance is given in Gpc (10^9

pc) and mass in units of $2.09 \times 10^{22} M_{\odot}$. By comparing these results with the analytical ones shown in figure 1 we can see that the numerical scheme produces the expected results.

- Figure 3: Numerical integration of the null geodesic in the Einstein-de Sitter model. Time is in units of 3.26 Gyr.
- Figure 4: Numerical integration of the equation (19) which gives the function $I(r)$ in the Einstein-de Sitter model.
- Figure 5: The same results of figure 2 for the Einstein-de Sitter model, but with all steps visible. The numerical code takes an excessive number of steps around the origin to integrate this model, despite the smoothness of the integrated functions $t(r)$ and $I(r)$ shown in figures 3 and 4, respectively. The solution in this graph shows clearly the stiff behaviour of equations (11) and (19) at around $r = 0$ in this model.
- Figure 6: Numerical results of $\log \rho_v$ versus $\log d_l$ in an open Friedmann model. Very small steps are omitted and so stiffness is not visible. From now on the figures will not have visible stiff behaviour to avoid saturation.
- Figure 7: Results of ρ_v plotted against d_l for the integrations of a recollapsing Friedmann model.
- Figure 8: Numerical results of the parabolic model obtained with functions (38) integrated in the interval $0 \leq r \leq 2$ and its straight line fitting carried out according to equation (37). The constants took the values $\alpha = 10^{-5}$, $p = 0.9$, $\beta_0 = 2$, $\eta_0 = 50$, $q = 0.65$ and the resulting fitting coefficients are $a_1 = -5.5$ and $a_2 = -1.6$. Considering equation (25) the fitting coefficients tell us that the fractal dimension of the dust in this model is $D = 1.4$ and the lower cutoff constant is $\sigma = 2.8 \times 10^6$.
- Figure 9: Results of ρ_v and d_l for the integration of the parabolic model with functions (39) in the interval $0 \leq r \leq 5$. The constants used had the values: $\alpha = 10^{-4}$, $p = 0.5$, $\beta_0 = 1.5$, $\eta_1 = 1000$. The fitted straight line is also visible

and the resulting fitting coefficients are $a_1 = -3.9$ and $a_2 = -1.3$, which means a fractal dimension $D = 1.7$ and a lower cutoff constant $\sigma = 9.7 \times 10^7$.

Figure 10: Distance-redshift diagram obtained by integrating the parabolic model of functions (38). Note the absence of a linear relation between the luminosity distance d_l and the redshift z . This fact makes this model observationally unrealistic.

Figure 11: Distance-redshift diagram obtained by integrating the parabolic model of functions (39). The diagram is only partially linear, but even so the Hubble constant associated with this part is just at or below the lower limit for H_0 . This point implies that functions (39) are not a good modelling for the observations.

Figure 12: Volume density ρ_v vs. luminosity distance d_l for the integration of the elliptic model given by functions (40) in the interval $0.001 \leq r \leq 0.07$. The constants took the values $\alpha = 10$, $p = 1.4$, $\beta_0 = 0.7$, $\eta_0 = 50$, $q = 0.65$ and the resulting fitting coefficients are $a_1 = -2.7$ and $a_2 = -1.3$, which means $D = 1.7$ for this model.

Figure 13: Volume density ρ_v vs. luminosity distance d_l for the integration of the elliptic model given by functions (41) in the interval $0.001 \leq r \leq 0.07$. The constants used had the values: $\alpha = 10$, $p = 1.4$, $\beta_0 = 0.7$, $\eta_1 = 1000$. The fitting coefficients obtained are $a_1 = -2.4$ and $a_2 = -1$. The model has fractal dimension $D = 2$.

Figure 14: Distance-redshift diagram obtained by integrating the elliptic fractal model produced by functions (40). The diagram is not linear which makes the model incompatible with observations.

Figure 15: Distance-redshift diagram obtained by integrating the elliptic fractal model produced by functions (41). The diagram can be approximated to a linear relation, but that produces a too low value for H_0

- Figure 16: Plot of the results of ρ_v vs. d_l obtained by the numerical integration in the interval $0 \leq r \leq 0.07$ of the hyperbolic model constructed with functions (42). The values of the constants used to find these results are $\alpha = 10^{-4}$, $p = 1.9$, $\beta_0 = 3.6$, $\eta_0 = 50$, $q = 0.65$ and the fitting coefficients obtained are $a_1 = -7.3$ and $a_2 = -1.6$.
- Figure 17: Distance-redshift diagram obtained with the hyperbolic model of functions (42). The diagram is approximately linear but the associated Hubble constant of about 23 km/s/Mpc is too low comparing with the current uncertainty of H_0 .
- Figure 18: Plot of the results of ρ_v vs. d_l obtained by the numerical integration in the interval $0 \leq r \leq 0.07$ of the hyperbolic model constructed with functions (43). The constants used to find these results are $\alpha = 10^{-4}$, $p = 1.4$, $\beta_0 = 3.6$, $\eta_1 = 1000$. The fitting coefficients obtained are $a_1 = -6.2$ and $a_2 = -1.7$. These coefficients mean a fractal dimension $D = 1.3$ and a lower cutoff constant $\sigma = 5.4 \times 10^5$.
- Figure 19: Distance-redshift diagram obtained with the hyperbolic model consisted of functions (43). This is one of the best linear approximation for a d_l vs. z diagram and the slope gives $H_0 \cong 61$ km/s/Mpc, a value within the current uncertainty in the Hubble constant.
- Figure 20: Results of the volume density ρ_v vs. luminosity distance d_l of the hyperbolic model (44) with simultaneous big bang. The integration is in the interval $0 \leq r \leq 0.07$ and the constants are $\alpha = 10^{-4}$, $p = 1.4$, $\beta_0 = 3.6$. The fitting coefficients calculated are $a_1 = -6.0$ and $a_2 = -1.6$, giving a fractal dimension $D = 1.4$ and a lower cutoff constant $\sigma = 8.7 \times 10^5$.
- Figure 21: Distance-redshift diagram obtained with the hyperbolic model of functions (44). This is the best diagram obtained for d_l vs. z and the slope gives $H_0 \cong 80$ km/s/Mpc, a value which is not only within the current uncertainty in the Hubble constant but also agrees with recent measurements on it (see Peacock 1991).

Figure 22: Plot of the results for the cumulative number counting N_c vs. the redshift z given by the integration of the model (44) with the same parameters as in figure 20.

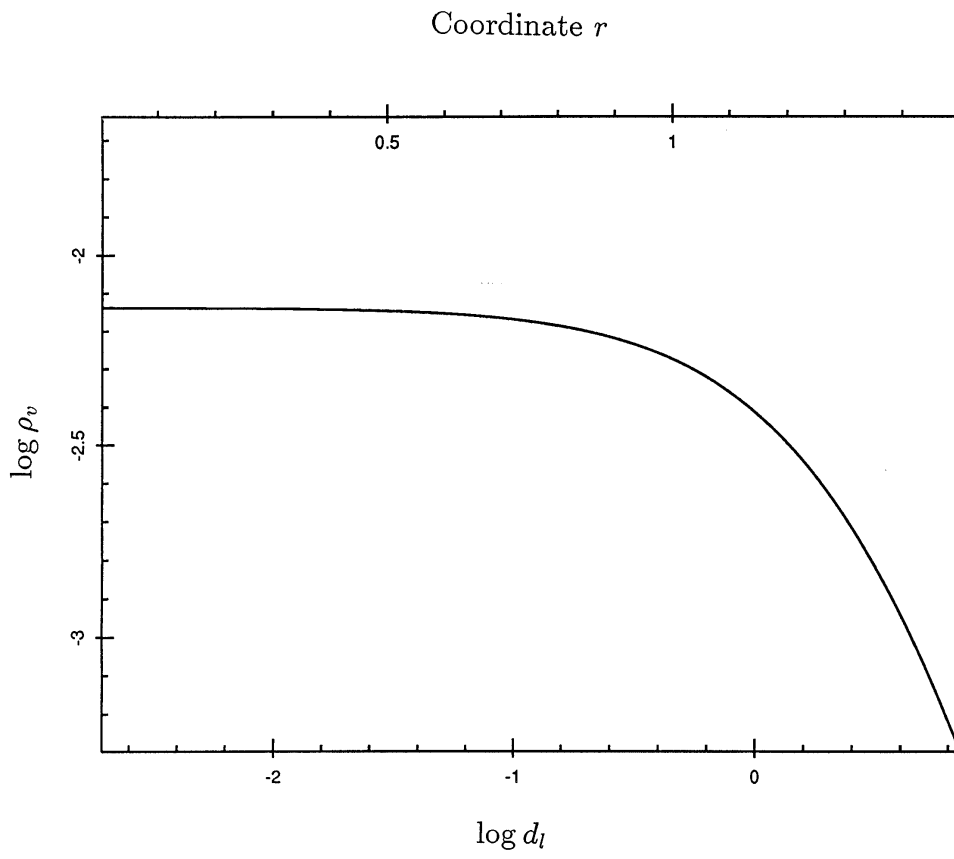


Figure 1

FIGURE 2

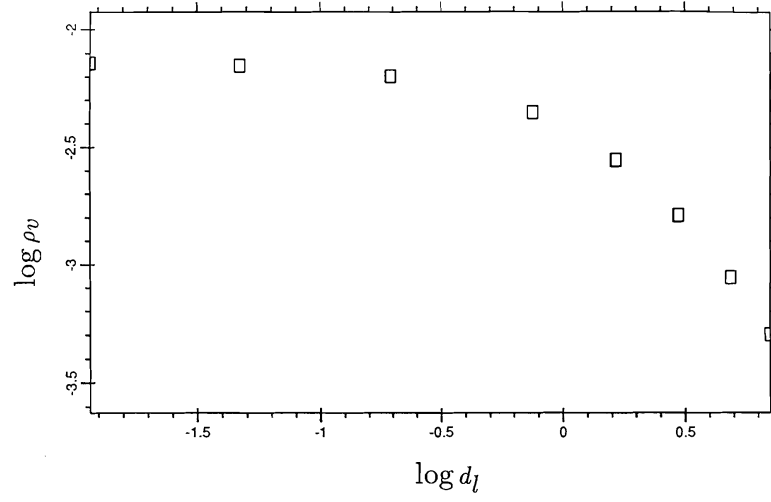


FIGURE 3

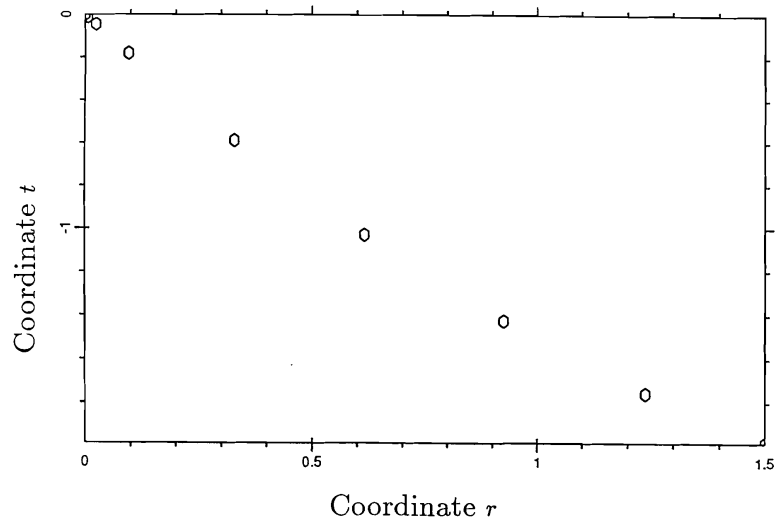


FIGURE 4

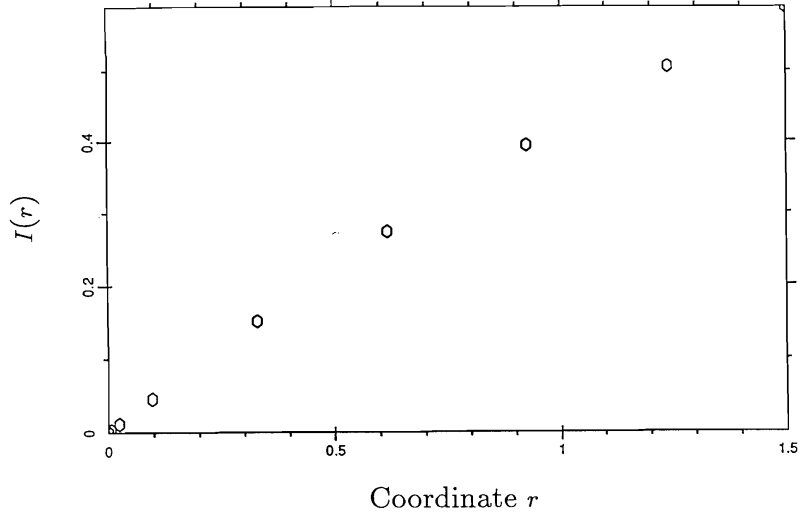


FIGURE 5

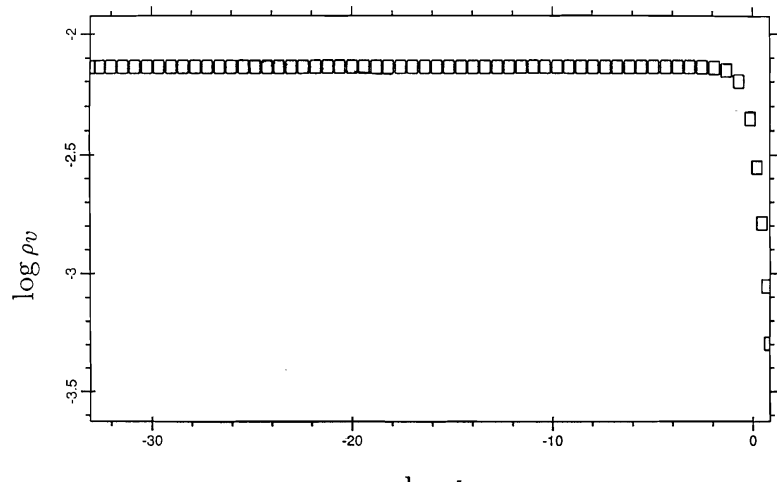


FIGURE 6

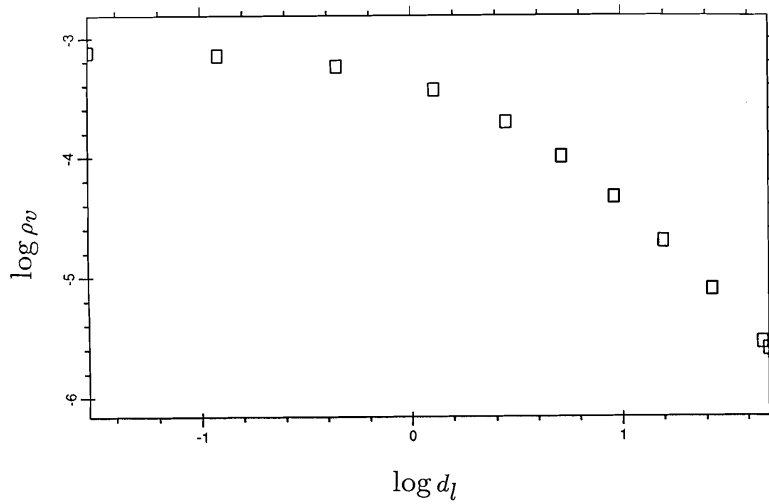


FIGURE 7

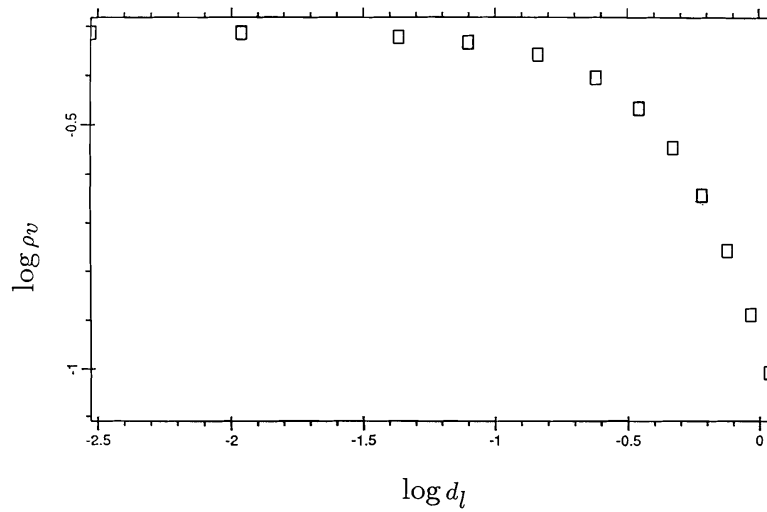


FIGURE 8

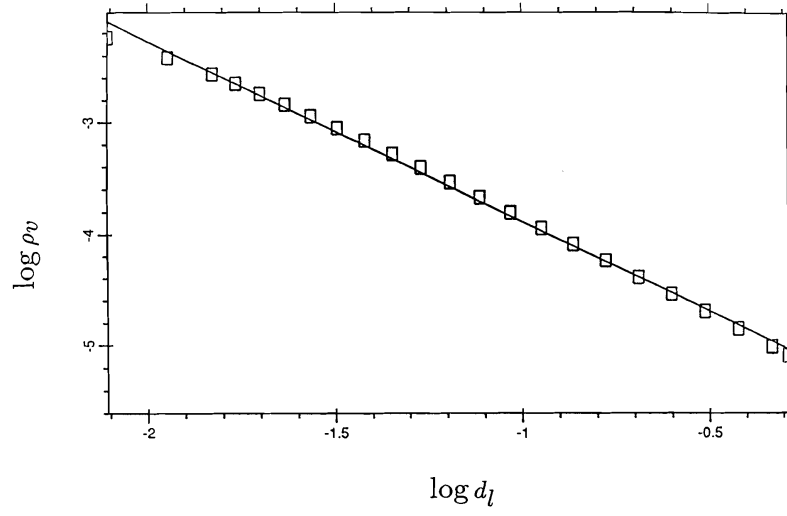


FIGURE 9

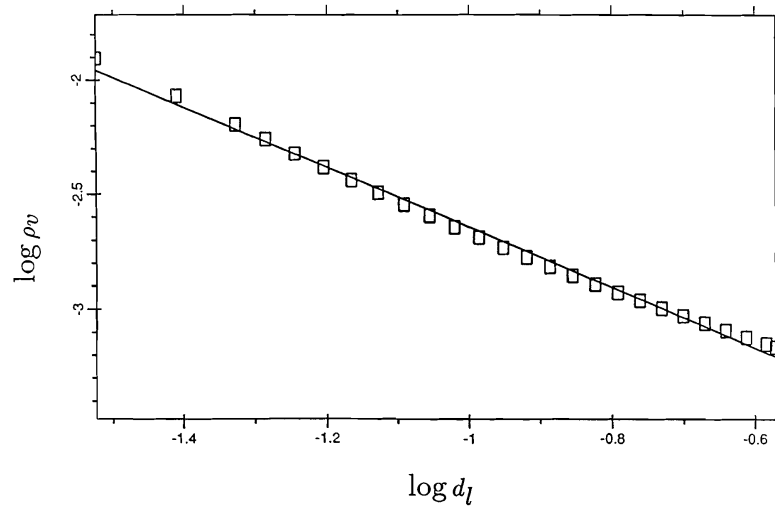


FIGURE 10

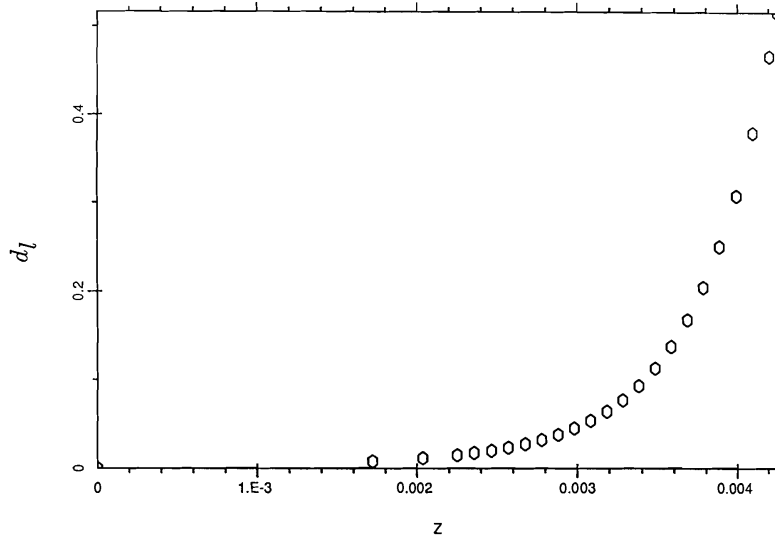


FIGURE 11

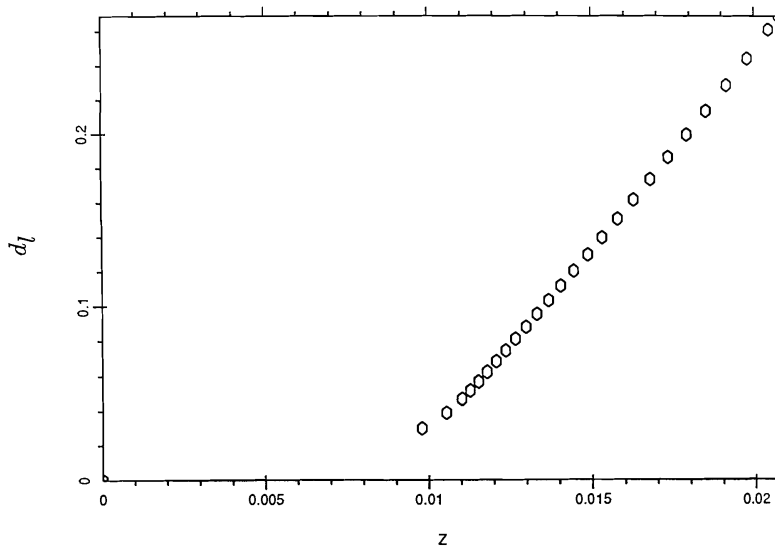


FIGURE 12

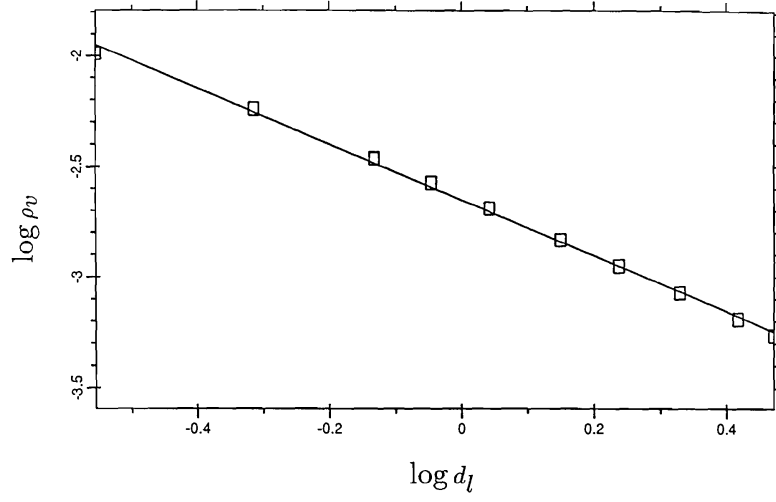


FIGURE 13

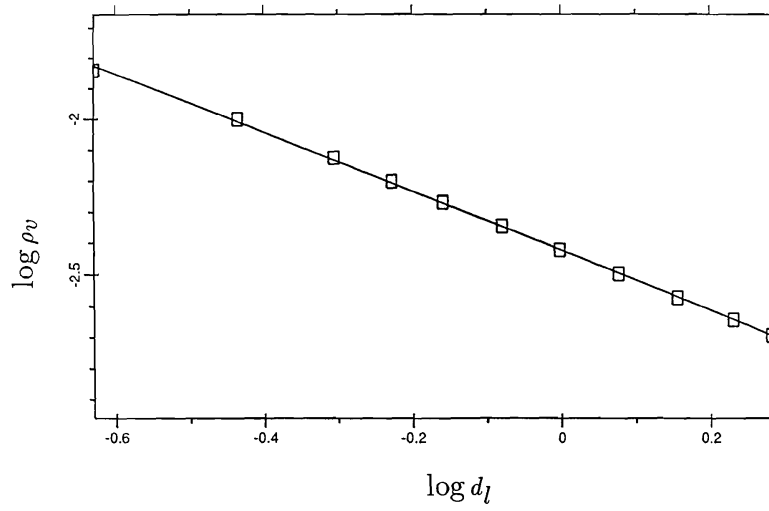


FIGURE 14

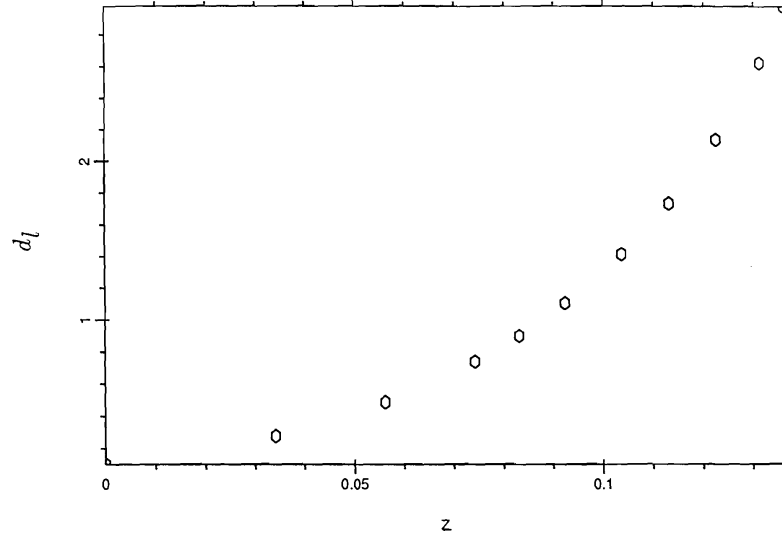


FIGURE 15

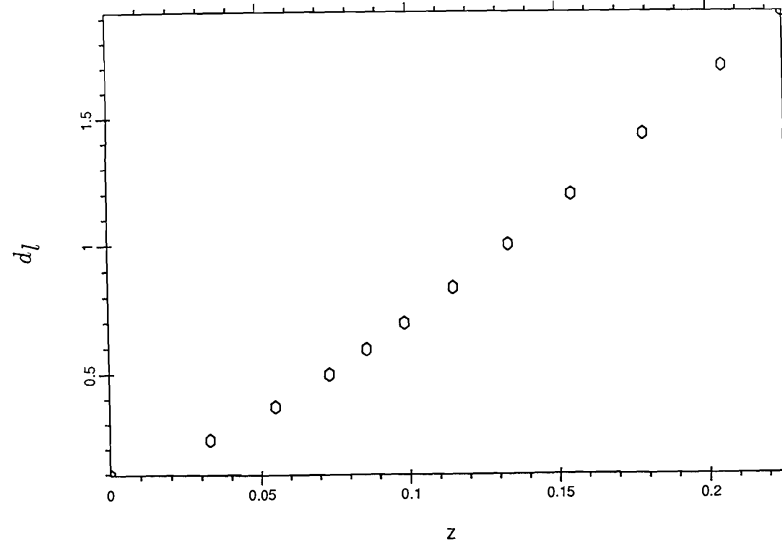


FIGURE 16

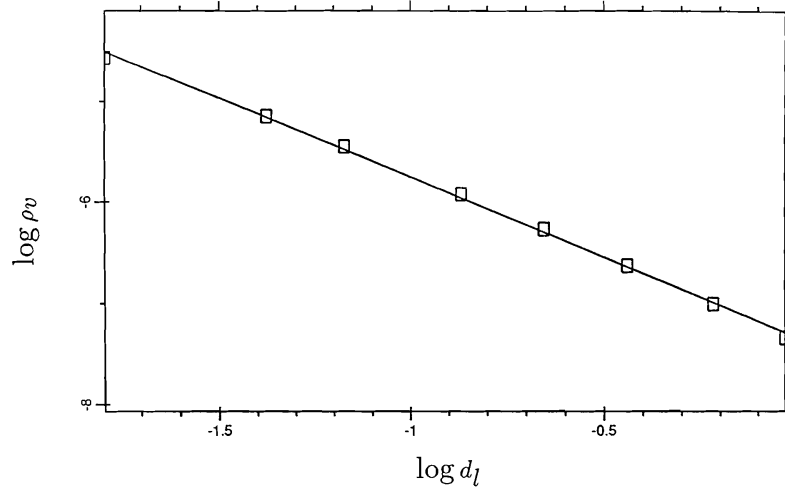


FIGURE 17

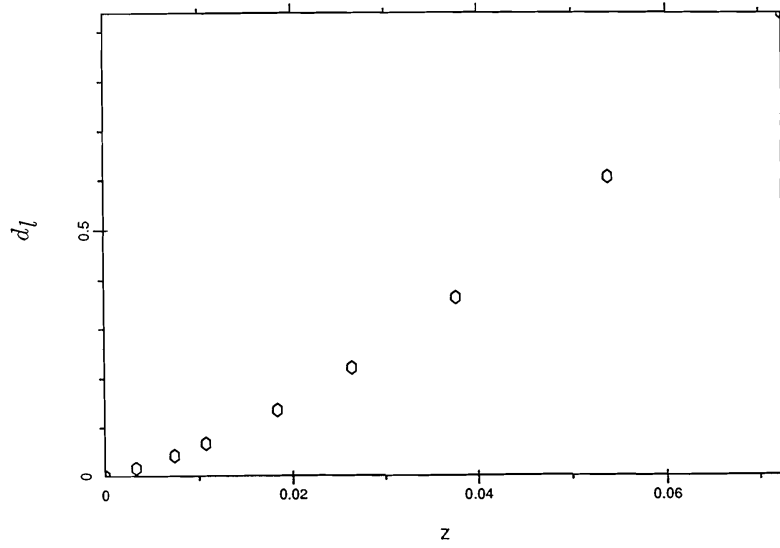


FIGURE 18

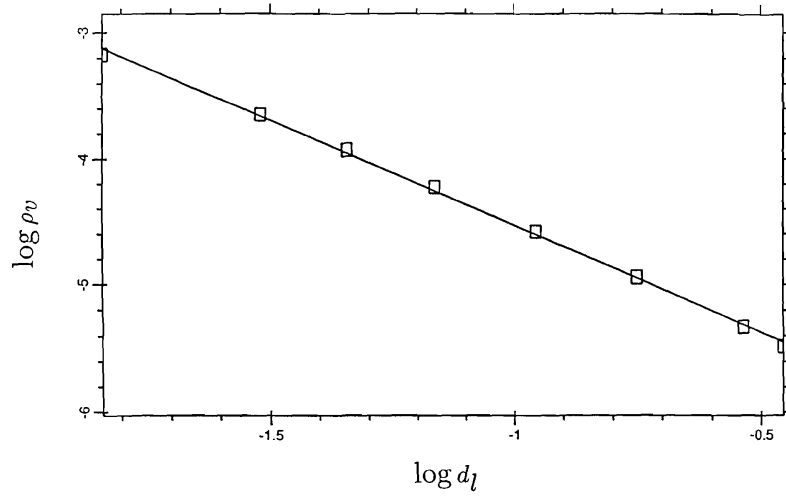


FIGURE 19

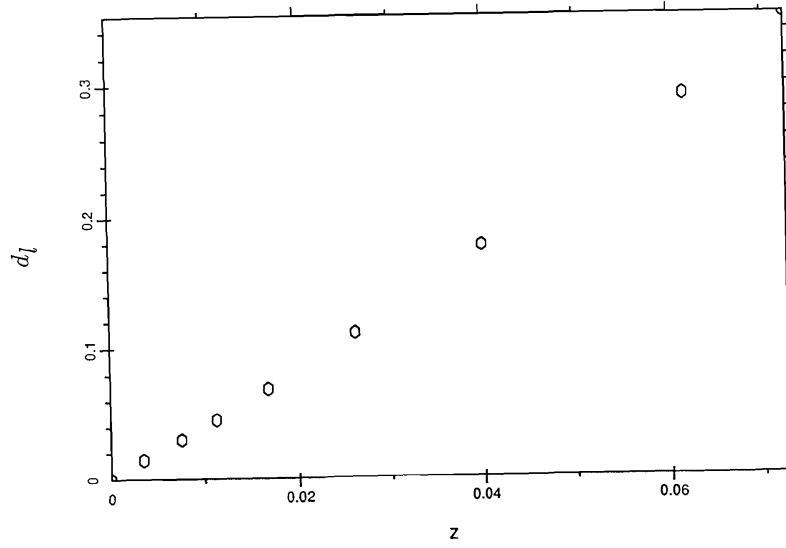


FIGURE 20

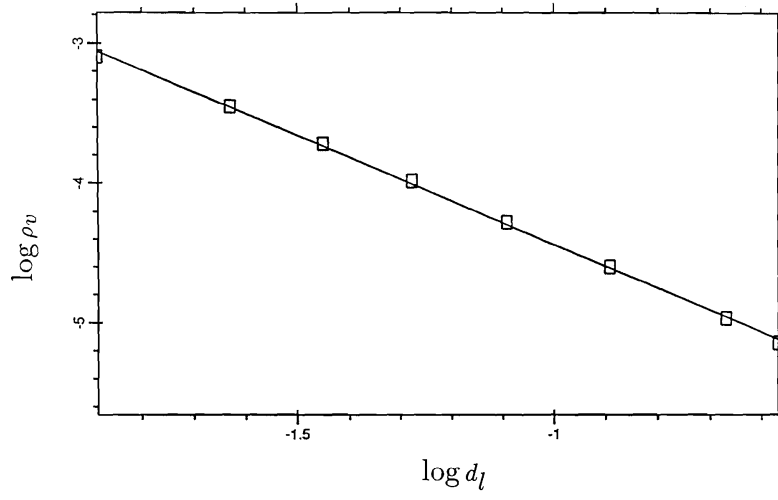


FIGURE 21

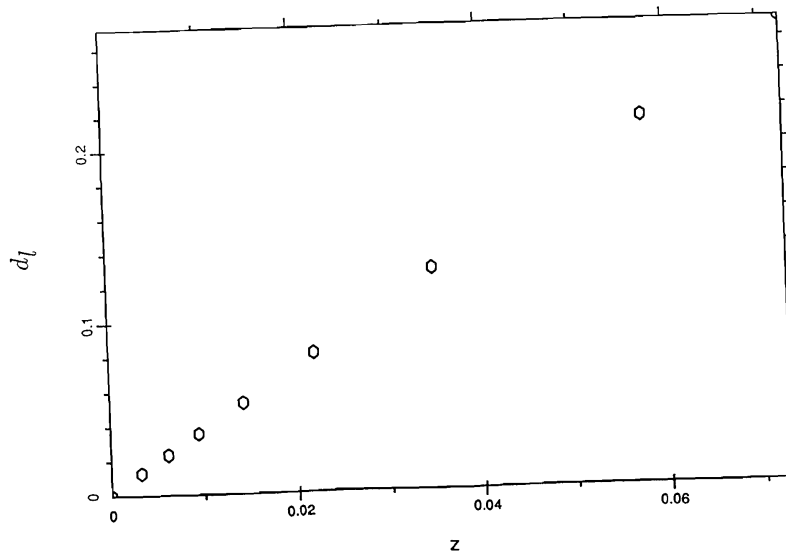


FIGURE 22

